SLAC-PUB-2004
August 1977
(T/E)

STUDY OF $K\pi$ SCATTERING USING THE REACTIONS $K^{\pm}p \to K^{\pm}\pi^{+}n$ AND $K^{\pm}p \to K^{\pm}\pi^{-}\Delta^{++}$ AT 13 GeV/c*

P. Estabrooks
McGill University, Montreal, Canada

R. K. Carnegie
Carleton University, Ottawa, Canada

A. D. Martin
University of Durham, Durham City, England

W. M. Dunwoodie, T. A. Lasinski, and D.W.G.S. Leith
Stanford Linear Accelerator Center
Stanford University, Stanford, California 94305

(Submitted to Nucl. Phys.)

*Work supported by the National Research Council of Canada and the Energy Research and Development Administration of the United States.

ABSTRACT

An elastic $K\pi$ partial wave analysis is presented. It is based on high statistics data for the reactions $K^{\pm}p \rightarrow K^{\pm}\pi^{+}n$ and $K^{\pm}p \rightarrow K^{\pm}\pi^{-}\Delta^{++}$ at 13 GeV obtained in a spectrometer experiment performed at SLAC. For each reaction, a t-dependent parametrization of the production amplitudes provides information on both the $K\pi$ mass dependence of the production mechanisms and on $K\pi$ scattering. Knowledge of the t-dependence then allows a calculation of the $K\pi$ partial wave amplitudes for $K\pi$ masses from 0.7 to 1.9 GeV. The results of such analyses using data for (i) the neutron recoil reactions, (ii) the Δ^{++} recoil reactions, and (iii) both neutron and Δ^{++} recoil reactions simultaneously are presented. Besides the leading $J^P=1^-$, 2^+, and 3^- resonances at $M_{K\pi}$=.896, 1.434, and 1.78 GeV, there is evidence in two of the four possible partial wave solutions for a broad P-wave resonant-like structure in the region of 1700 MeV. The I=1/2 S-wave magnitude rises slowly and smoothly to a maximum near 1400 MeV, but then decreases rapidly between 1400 and 1600 MeV. This structure is strongly indicative of an S-wave resonance near 1450 MeV. The charge two $K\pi$ reaction is dominated by S-wave scattering with a total cross section decreasing from 4 mb at 0.9 GeV to 2 mb at 1.5 GeV. Both the I=1/2 S-wave below 1400 MeV and the I=3/2 S-wave are well described by an effective range parametrization.

1. Introduction

In this paper we describe a $K\pi$ partial wave analysis using the high statistics SLAC 13 GeV/c spectrometer data [1] on the four reactions

$$K^-p \to K^-\pi^+n \quad (1)$$

$$K^+p \to K^+\pi^+n \quad (2)$$

$$K^+p \to K^+\pi^-\Delta^{++} \quad (3)$$

$$K^-p \to K^-\pi^-\Delta^{++} \quad (4)$$

For each reaction, examination of the t-dependence at fixed $K\pi$ mass, $M_{K\pi}$, of the spherical harmonic moments, Y_M^L, of the $K\pi$ angular distribution enables us to isolate the π exchange contribution and also to develop an adequate parametrization of the momentum transfer dependence of the other possible exchanges [2,3]. Armed with this information, we can then perform meaningful $K\pi$ partial wave analyses of the data on reactions (1) to (4) in single wide t bins ($-t' < .15$ GeV^2 for reactions (1), (2), and (4) and $-t' < 0.2$ GeV^2 for reaction (3)). Although the behavior of the data as a function of momentum transfer is very different for the neutron and delta recoil reactions, we find that this procedure enables us to use the $K\pi$ moments in the physical region to calculate $K\pi$ partial wave amplitudes which are independent of the nature of the particle recoiling against the $K\pi$ system. We can therefore perform joint $K\pi$ partial wave analyses of both $K^\pm\pi^+n$ and $K^\pm\pi^-\Delta$ physical region moments, which take into account the different momentum transfer structure of the two reactions while requiring a common $K\pi$ scattering amplitude. It is this analysis which provides our best determination of $K\pi$ scattering.

In Section 2 we discuss the experimental data selection and present $K\pi$ mass spectra and unnormalized M=0 moments for all 4 reactions at small momentum transfer. In Section 3 we investigate the t-dependence of both neutron and Δ^{++}

recoil reactions. This makes possible the partial wave analysis of physical region moments which is presented in Section 4 for both neutron and Δ^{++} recoil reactions, first individually and then jointly. The I=3/2 $K\pi$ scattering obtained directly from the analyses of reactions (2) and (4) is found to be dominated by the S wave. The analysis of reactions (1) and (3) yields a unique partial wave solution for $M_{K\pi} < 1.46$ GeV which exhibits the 1^- K*(890) and 2^+ K*(1435) resonances and an I=1/2 S wave cross section that rises smoothly to a maximum near 1400 MeV. However, for higher $K\pi$ mass we find several possible solutions which we classify in terms of the zero structure of the scattering amplitude. Each solution contains a broad spin-parity 3^- resonance [4]; the solutions differ in the structure of the nonleading partial waves. In Section 5 we present Argand plots of the $K\pi$ partial wave amplitudes for all four solutions and discuss the implications of this analysis on the nature of the natural spin-parity strange meson spectrum. All four solutions indicate the existence of a 0^+ κ meson which differs from and lies at a higher mass (~1425 MeV) than the traditional κ meson previously discussed in the literature. In addition two of the solutions imply the existence of a 1^- K* meson near 1675 MeV.

2. The Experiment

The experiment was performed at SLAC using 13 GeV rf separated $K^{\pm}$ beams incident on a 1 m hydrogen target. A forward wire spark chamber spectrometer [5] was used to detect the outgoing K and π.

Events corresponding to the neutron recoil reactions (1) and (2) and the Δ^{++} recoil reactions (3) and (4) were selected by requiring that the missing mass opposite the $K\pi$ system lie in the range $0.75 < MM < 1.05$ GeV for the neutron reactions and $1.0 < MM < 1.4$ GeV for the delta reactions. In addition for the two neutron recoil reactions (1) and (2), a direct experimental subtraction was made

to correct the experimental angular distributions for events associated with the small $K^-p \to K\pi\Delta^0$ background occurring in this neutron missing mass interval [6]. In the case of the Δ^{++} recoil reactions [1], the experimental missing mass spectrum from 1.0 to 1.6 GeV was fitted to a Breit-Wigner Δ resonance plus a polynomial background. The $K\pi$ cross sections were then corrected to correspond to the Δ^{++} resonance contribution only.

A multicell Cerenkov counter was used to provide K/π identification for the doubly charged $K\pi$ systems in reactions (2) and (4). For reactions (1) and (3), positive K/π identification was not necessary. Instead events that were ambiguous with a forward K^0, Λ, or in the case of reaction (1), the reactions $K^-p \to \phi\Lambda, \rho\Lambda$, were explicitly rejected. In the case of reaction (1), events for which the πn invariant mass was less than 2.0 GeV were also rejected. The experimental data samples contain 51,000 and 14,400 events respectively for reactions (1) and (2) and 104,000 and 26,000 for reactions (3) and (4). In addition, very large samples of $K^\pm \to \pi^\pm\pi^+\pi^-$ beam decays were obtained simultaneously with the $K\pi$ data and provided a direct measurement of the K^+/K^- relative normalization which is known to $\pm 2\%$.

A maximum likelihood fitting procedure is used to correct the observed $K\pi$ data for the effects of the spectrometer acceptance, event selection criteria, and other factors. This yields acceptance corrected reaction cross sections and the spherical harmonic moments, Y_{LM}, of the $K\pi$ angular distribution as a function of $K\pi$ mass and four momentum transfer, t' $(=t-t_{min})$. The resulting $K\pi$ mass spectra and the t channel unnormalized M=0 moments are presented in Figs. 1-4 as functions of $K\pi$ mass for the small momentum transfer region for each of the four reactions. The momentum transfer cuts are $|t'| < 0.15$ GeV^2

for reactions (1), (2) and (4) and $|t| < 0.2$ GeV^2 for reaction (3). The errors shown are the statistical errors only.

The $K^+\pi^+n$ cross section is substantial; it rises smoothly from threshold to a broad maximum near 1.6 GeV. The $K^-\pi^-\Delta^{++}$ cross section exhibits a noticeably different $K\pi$ mass dependence and appears to remain roughly constant over this mass range. This apparently different mass variation in fact reflects the different neutron and Δ^{++} recoil momentum transfer dependence and particularly the rapid increase in t_{min} with $K\pi$ mass that occurs for the Δ^{++} reaction.

The fits to the $K^+\pi^+n$ and those to the $K^-\pi^-\Delta^{++}$ data were performed with L, $M \leq 2$. Separate fits indicated that higher L moments were not required to describe these data. Indeed the L=1 and L=2 moments in Figs. 2 and 4 are quite small indicating that the I=3/2 $K\pi$ system is predominantly S wave. For the $K^-\pi^+n$ and $K^+\pi^-\Delta^{++}$ data, the maximum L value used in the fits increased from L=2 to L=6 with increasing $K\pi$ mass, as indicated in Figs. 1 and 3, with $M \leq 2$ for all masses. $L \leq 4$ moments are required to describe the K*(1435) region, and the $L \leq 6$ moments are necessary above 1.6 GeV. The prominent features of the $K^-\pi^+$ and $K^+\pi^-$ distributions are due to the 1^- K*(890) and 2^+ K*(1435) mesons. In addition, as reported previously [4], these data have been used to demonstrate the presence of a broad spin-parity 3^- K* resonance at ~1.78 GeV.

3. $K\pi$ Production

Both neutron and Δ recoil reactions are historic sources of information on $K\pi$ phase shifts [7,8]. Although the π exchange contribution to the Δ recoil reactions does not vanish at t=0 as it must do in the neutron recoil reactions, this advantage is counterbalanced by several disadvantages: (i) the difficulty, in the absence of a direct measurement of the recoil system, of cleanly isolating the broad Δ resonance from the background in the missing mass spectrum;

(ii) kinematic reflections from the diffractive Q production reactions, expected [1] to be important at low $M_{K\pi}$; and (iii) the rapid increase of t_{min} with increasing $M_{K\pi}$ in the Δ reactions. At $M_{K\pi} = 1.5$ GeV, $t_{min} = -.06$ GeV^2 for $p_{lab} = 13$ GeV/c, so that, in a t' region $0 < -t' < .2$ GeV^2, one can see only about 20% of the π exchange. (iv) Moreover, the Δ recoil reactions are intrinsically more complicated than the neutron ones, due to the doubling of possible recoil helicity states. We discuss the $K\pi n$ production mechanisms in Section 3.1 and $K\pi\Delta$ production in Section 3.2.

3.1 $K\pi$ Production in $Kp \to K\pi n$

The extraction of $K\pi$ scattering amplitudes from these data requires isolating the π exchange contribution to the production amplitude. Data at 4 GeV [9] for the line reversed reactions

$$\begin{aligned} K^- p &\to \bar{K}^*(890) n \\ K^+ n &\to K^*(890) p \end{aligned} \qquad (5)$$

have provided valuable information about the K*(890) production mechanisms. In ref. [10] it was shown that these two reactions could be simply described in terms of strongly exchange degenerate π-B and A_2-ρ Regge exchanges and 'cuts' (non-evasive contributions, absorptive corrections...) which have simple t-channel structure. We have shown [2] that for K*(890) and K*(1435) production in reaction (1) at 13 GeV, a good description of the momentum transfer dependence of the data is also provided by this simple exchange model. Moreover, the $M_{K\pi}$ dependence of the ratios of non-pi/pi exchanges was seen to be almost identical to that observed in $\pi N \to \rho N$ compared with $\pi N \to fN$ [11].

For each $K\pi$ mass interval, we parametrize the t dependence of the amplitudes $L_{\lambda\pm}$ for production of a $K\pi$ state with angular momentum L, t channel

helicity λ, by natural (+) or unnatural (-) parity exchange by

$$
\begin{aligned}
L_0 &= g_L \frac{\sqrt{-t}}{\mu^2 - t} \\
L_{1-} &= \frac{1}{\sqrt{2}} g_L \sqrt{L(L+1)}\ \gamma_C \\
L_{1+} &= \frac{1}{\sqrt{2}} g_L \sqrt{L(L+1)} \left[\gamma_C + 2 \begin{Bmatrix} -i \\ 1 \end{Bmatrix} \gamma_A |t'|\right] \\
L_{\lambda\pm} &= 0 , \qquad \lambda \geq 2
\end{aligned}
\tag{6}
$$

where $\begin{Bmatrix} -i \\ 1 \end{Bmatrix}$ refers to an incident K^- or K^+. For partial wave analysis, we are only concerned with small t, e.g., the $|t| < 0.2\ \mathrm{GeV}^2$ region. The simplified parametrization of Eq. (6) is a good small $|t|$ approximation to the more general description used in ref. [2]. The relation of g_L to the $K\pi$ scattering amplitudes, a_L, is given by

$$
g_L = \mathcal{N}^n_{0(2)} \frac{M_{K\pi}}{\sqrt{q}} a_L e^{b(t-\mu^2)} \tag{7}
$$

where the subscript on $\mathcal{N}$ refers to the net $K\pi$ charge, the superscript to the recoil particle. The $K\pi$ scattering amplitudes are written* as

$$
a_L = \sqrt{2L+1}\ \epsilon_L \sin\delta_L\, e^{i\delta_L} \tag{8a}
$$

in the elastic region, and

$$
a_L = |a_L|\, e^{i\phi_L} \tag{8b}
$$

in the inelastic region. Requiring purely elastic scattering corresponds to setting $\epsilon_L = 1$. The normalization constant, $\mathcal{N}^n_0$, is determined by requiring the

*For $K^-\pi^+$ scattering, we use $a_L \equiv a^1_L + \frac{1}{2} a^3_L$ where the superscripts refer to twice the $K\pi$ isospin and the a^{2I}_L are given by Eq. (8) for elastic scattering. The isospin Clebsch-Gordan coefficient of $\frac{2}{3}$ has been absorbed into the definition of $\mathcal{N}_0$.

$K^-\pi^+$ P wave in the 900 MeV region to be an elastic Breit-Wigner resonance. The K^+ normalization constant, $\mathcal{N}_2^n$, is then fixed by the relative K^- and K^+ experimental normalizations and the value of $\mathcal{N}_0^n$. We have also calculated $\mathcal{N}_0^n$ from the absolute experimental normalization and the Chew-Low equation [12]. This gives a value some 10% larger than that obtained from the requirement that the K*(890) be elastic.

The parametrization of Eq. (6) provides a good description of the t dependence of the moments, $N<Y_M^L>$, of the $K^-\pi^+$ angular distribution in all $M_{K\pi}$ bins. In Fig. 5a both the data and the results of the t-dependent fits are shown for $-t' < 0.2$ GeV^2 for the $0.94 < M_{K\pi} < 1.0$ GeV bin. We have checked that performing the fits for $-t' < 0.3$ GeV^2 does not significantly change the values of the parameters.

In Fig. 6a, the values of the production parameters* b, γ_C, γ_A, describing the t-dependence are plotted as functions of $K^-\pi^+$ mass. For the $K^+\pi^+$ reaction, only the S wave is significantly nonzero and so b is the only reliably determined parameter. Its values are represented by the open circles in Fig. 6 and are seen to be in agreement with the $K^-\pi^+$ results (solid points). We note that the ρ-A_2 and cut contributions become increasingly important with decreasing $K\pi$ mass.

In the course of describing the t dependence of the $K\pi$ production using Eqs. (6), we also obtain results for the $K\pi$ scattering amplitudes. The I=3/2 S wave phase shifts, δ_S^3, obtained by imposing elastic unitarity in the fits to the t dependence of the $K^+\pi^+$ moments are shown as open circles in Fig. 7a. The exotic P and D waves were found to be consistent with zero, $\delta_P^3 = \delta_D^3 = 0$. The

*These parameters were obtained from fits in which ϵ_s of Eq. (8) was left as a free parameter while ϵ_p was set equal to 1.0.

I=1/2 phase shifts, δ_S^1 and δ_P^1, in the elastic region, $M_{K^-\pi^+} < 1.3$ GeV, are shown by the open circles in Fig. 8a.

3.2 $K\pi$ Production in $Kp \to K\pi\Delta^{++}$

Isolation of the π exchange contributions to the Δ^{++} recoil reactions (3) and (4) is complicated by the larger number of possible helicity states of the Δ. We use $L_{\Delta N}^{\lambda\pm}$ to represent the amplitude for angular momentum L, helicity λ $K\pi$ production by natural (+) or unnatural (-) parity exchange with Δ helicity of $\frac{\Delta}{2}$ and with $N = \pm$ corresponding to proton helicity of $\pm 1/2$. We have shown in ref. [3] that the momentum transfer and K* helicity structure of K*(890) and K*(1435) production in reaction (3) can be well described by (i) strongly exchange degenerate π-B Regge exchanges coupling only to the t-channel amplitudes L_{1+}^0 (and L_{-1-}^0); (ii) EXD ρ-A_2 contributions coupling to the t-channel spin flip amplitudes L_{3+}^{1+} and L_{1-}^{1+} in the ratio $L_{3+}^{1+} = \sqrt{3}\, L_{1-}^{1+}$, as expected from the Stodolsky-Sakurai model [13] of ρ exchange; and (iii) nonfactorizing 'cut' contributions to the s-channel net helicity nonflip amplitudes ${}^{(s)}L_{3+}^1$ and ${}^{(s)}L_{1-}^1$. For K*(890) and K*(1435) production, the $M_{K\pi}$ dependence of the ratios of non-pi/pi exchanges was seen to be almost identical to that observed in $\pi N \to \pi\pi N$ and in $KN \to K\pi N$.

For each $M_{K\pi}$ interval, we parametrize the π-B contributions to the (t-channel) amplitudes as

$$L_{1+}^0(\pi\text{-B}) = g_L \frac{\sqrt{(M_\Delta - M_N)^2 - t}}{\mu^2 - t} \tag{9}$$

while the ρ-A_2 contributions are given by

$$L_{1-}^{1+}(\rho\text{-}A_2) = \frac{1}{\sqrt{3}} L_{3+}^{1+}(\rho\text{-}A_2) = \sqrt{2}\ \gamma_A(-t')\ \sqrt{L(L+1)}\ g_L \tag{10}$$

where g_L is given by Eq. (12) below. The factor of $\sqrt{3}$ is motivated by the Stodolsky-Sakurai model. In addition to the pole exchange contributions of equations (9) and (10), all t-channel amplitudes also have contributions obtained by crossing the s-channel cut contributions, parametrized as

$$(s)_L{}^1_{1-} = \frac{1}{\sqrt{3}} (s)_L{}^1_{3+} = \frac{1}{\sqrt{2}} g_L \sqrt{L(L+1)}\ \gamma_C \tag{11}$$

to the t-channel. In general, the cut contributions to the two different s-channel amplitudes need not be related by the $\sqrt{3}$ of Eq. (11), but we found that the data at small $|t'|$ could not determine the ratio of the two cuts so we chose to relate them as in Eq. (11). The simplified parametrization of Eqs. (9) - (11) is a good small $|t|$ approximation to the more general description used in ref. [3]. The $K\pi$ scattering amplitudes, a_L, of Eq. (8) are related to g_L by

$$g_L = \mathcal{N}_{0(2)}^{\Delta} \frac{M_{k\pi}}{\sqrt{q}} a_L\, e^{b_L(t-\mu^2)} \tag{12}$$

As in the neutron recoil reactions, $\mathcal{N}_0^{\Delta}$ is determined by requiring the $K^+\pi^-$ P-wave in the 900 MeV region to be an elastic Breit-Wigner resonance; $\mathcal{N}_2^{\Delta}$ is then calculated from $\mathcal{N}_0^{\Delta}$ and the relative K^- and K^+ experimental normalizations.

The parametrization of Eqs. (9) - (12) provides a good description of the small t behavior of the moments, $N\langle Y_M^L\rangle$, of the $K^+\pi^-$ angular distribution in all $M_{K\pi}$ bins, as demonstrated, for example, in Fig. 5b for the $0.94 < M_{K\pi} < 1.0$ GeV bin. In fact, we find that all the b_L of Eq. (12) cannot be determined from the small t' data, so we set $b_F = b_D = b_P \equiv b$.

In Fig. 6b, the values of the production parameters* b_s, b, γ_c, γ_A describing the t-dependence are plotted as functions of $K^+\pi^-$ mass. For the

*These parameters were obtained from fits in which ϵ_s of Eq. (8) was left as a free parameter while ϵ_p was set equal to 1.0.

$K^-\pi^-$ reaction, only the S-wave is significantly nonzero so b_s, shown by the open circles in Fig. 6b, is the only reliably determined parameter. As in the $K\pi m$ case, these fits also produce $K\pi$ scattering amplitudes. The values of δ_s^3, and δ_s^1, δ_p^1 for $M_{K^+\pi^-} < 1.3$ GeV, resulting from fits with elastic unitarity imposed, are shown by the open circles in Figs. 7b and 8b, respectively.

4. Kπ Partial Waves from Single t Bin Analyses

A detailed study of the $K\pi$ partial waves as a function of $K\pi$ mass can be carried out by using the experimental $K\pi$ moments evaluated in small $K\pi$ mass intervals for a single wide momentum transfer bin in the π exchange dominated small t region. The procedure used to extract the $K\pi$ partial wave amplitudes from these single wide t bin $K\pi$ moments is presented in Section 4.1. The results of separate analyses of the purely I=3/2 $K^+\pi^+$ and $K^-\pi^-$ scattering are given in Section 4.2. Results from independent analyses of the $K^-\pi^+$ and $K^+\pi^-$ data in the elastic region ($M_{K\pi} < 1.3$ GeV) are presented in Section 4.3. In Section 4.4, after a discussion of the discrete ambiguity problem that occurs at higher $K\pi$ mass, we present the results of the separate $K^-\pi^+$ and $K^+\pi^-$ partial wave analyses in the inelastic region, $M_{K\pi} > 1.3$ GeV. Finally in Section 4.5, we present the results of a simultaneous partial wave analysis of both the neutron and delta recoil data, allowing for the different t-dependences of the two reactions.

4.1 Method of Analysis

Consideration of all the moments of the $K\pi$ angular distribution in a broad t bin permits a more detailed investigation of the $M_{K\pi}$ structure of the $K\pi$ partial wave amplitudes. The M=0 $K\pi$ moments to be used in the following analyses have been presented for reactions 1-4 in Figs. 1-4 respectively. The momentum transfer cuts used are $|t'| < 0.2$ GeV^2 for $K^+p \to K^+\pi^-\Delta^{++}$ and $|t'| < 0.15$ GeV^2

for the other reactions. The calculation of the $K\pi$ partial waves from these t averaged moments is straightforward since the t-dependence of each amplitude is known. The analytic form of the t-dependence is given by Eqs. (6) and (9)-(12). In the preceding section the values of the parameters contained in these expressions were determined at different values of $K\pi$ mass by independent fits to the observed t-dependence of the moments. In this section, we assume that the $K\pi$ mass dependence of these t structure parameters is given by low order polynomial fits to the independently determined points shown in Fig. 6. Thus the actual values of the t structure parameters used in the subsequent single t bin analyses correspond to the curves* shown in Fig. 6.

We have verified that the results obtained for the $K\pi$ partial waves are unaffected by this smoothing of the mass dependence of these parameters describing the t structure of the moments. This was done by repeating the charge zero $K\pi$ analyses of the previous section with the parameters b_s, b, γ_c, and γ_A fixed at values corresponding to the smooth curves in Fig. 6. We found no significant differences between the resulting phase shifts and those obtained in the previous section. This indicates that the correlation between small changes in the values of the parameters describing the production processes and the quantities which describe $K\pi$ scattering, the partial wave amplitudes, is quite small.

---

*Since b and b_s for the Δ^{++} recoil reactions are not very well determined at high $M_{K\pi}$, we assume that b and b_s have constant values of 0.5 and 1.5 respectively for reaction (3) for $M_{K\pi} > 1.5$ GeV. These values are consistent with those obtained in the t-dependent fits of Section 3.2.

The $K\pi$ moments in the t bin $0 < -t' < T$ can now be expressed in terms of the partial wave amplitudes, a_L, and t integrals, $\langle L'_\lambda L^*_\mu \rangle$, as demonstrated, for example, in the appendix† of ref. [14], where

$$\langle L'_\lambda L^*_\mu \rangle = \frac{\int_{-T}^{0} dt' \, L'_\lambda(t') \, L^*_\mu(t')}{a_{L'} \, a^*_L \, T} \tag{13}$$

In each $M_{K\pi}$ interval, the $\langle L'_\lambda L^*_\mu \rangle$ can be calculated explicitly and the a_L are then determined from a least squares fit to the $K\pi$ moments.

4.2 $K^+\pi^+$ and $K^-\pi^-$ Results

For $K^+\pi^+$ and $K^-\pi^-$, we assume elastic unitarity so that $|a_S|$ is just $|\sin \delta^3_S|$. The negative sign of δ^3_S is selected in the $K^-\pi^+$ and $K^+\pi^-$ partial wave analyses by requiring that the I=1/2 S wave be elastic in the low $M_{K\pi}$ region. The results for δ^3_S are shown as the solid points in Fig. 7a and b and can be seen to be in excellent agreement with those (open circles) obtained from the t-dependent fits of the previous section. Here also, the exotic P and D wave phase shifts are always smaller than three degrees for $M_{K\pi} < 1.8$ GeV. The $K^+\pi^+$ ($K^-\pi^-$) total cross section can be calculated at each $M_{K\pi}$ value using these phase shifts; the cross section decreases from 4.8 ± 0.7 (4.4 ± 0.4) mb at 0.9 GeV to 2.4 ± 0.3 (1.8 ± 0.2) mb at 1.6 GeV.

We have fitted these results for δ^3_S to an effective range form

$$q^{2L+1} \cot \delta^{2I}_L = \frac{1}{a^{2I}_L} + \frac{1}{2} r^{2I}_L q^2 \tag{14}$$

We find that δ^3_S is well described by Eq. (14) with the low energy $K\pi$ parameters shown in Table 1a; there is good agreement between the parameters calculated

†The conversion from the density matrices of ref. [14] to the notation used here is given by $\rho^{L'L}_{\lambda\mu} = \mathrm{Re}\left[a_{L'} \, a^*_L \langle L'_\lambda L^*_\mu \rangle\right]$.

from the $K^+\pi^+n$ phase shifts and those from the $K^-\pi^-\Delta^{++}$ analysis. These parameters yield the curves shown in Fig. 7.

4.3 Elastic $K^-\pi^+$ and $K^+\pi^-$ Results

In $K^-\pi^+$ and $K^+\pi^-$ scattering, the I=1/2 D wave is known to be inelastic [15]. The I=1/2 S and P waves could also become inelastic for $M_{K\pi} > 1.3$ GeV. Therefore we only impose elastic unitarity for $M_{K\pi} < 1.2$ GeV. The I=3/2 P and D wave phase shifts are assumed to be zero while the I=3/2 S wave is given by the effective range curves* of Fig. 7. In the region from 1.2 to 1.3 GeV, we require the P and I=1/2 S waves to be elastic but allow inelasticity in the D wave. Since the P wave is small (and not well determined) in this mass region, forcing it to be elastic is not overly restrictive. Thus, the imposition of elastic unitarity for S and P waves is, in practice, simply a prescription for determining the overall phase. The results for δ_S^1 and δ_P^1 in the region $0.7 < M_{K\pi} < 1.30$ GeV are shown by the solid points in Fig. 8. They are in good agreement with the (extrapolated in t) results (open circles) of the previous section. The curves on the δ_P^1 plot represent Breit-Wigner fits to the phase shifts

$$\frac{a_P}{\sqrt{3}} = \sin\delta_P^1 \, e^{i\delta_P^1} = \frac{M_R\Gamma}{M_R^2 - M_{K\pi}^2 - iM_R\Gamma}$$

$$\Gamma = \left(\frac{q}{q_R}\right)^3 \Gamma_R \left[\frac{1 + (q_R R)^2}{1 + (qR)^2}\right]$$

from 0.8 to 1.0 GeV. The resulting resonance parameters are listed in Table 1b; the $K^+\pi^-$ and $K^-\pi^+$ results are in good agreement. The K* widths quoted

*These are the exotic phase shift values which were also used in the t-dependent $K^-\pi^+$ and $K^+\pi^-$ analyses of the previous section.

have been corrected for the small effects of the experimental mass resolution, which is estimated to be ±5 MeV.

The curves on the S wave plots represent the results of effective range fits of the form of Eq. (14) to δ_S^1. The resulting low energy $K\pi$ parameters, listed in Table 1c, again demonstrate the excellent agreement between the $K^-\pi^+$ and $K^+\pi^-$ results. We note that, at every $M_{K\pi}$ value, there is another possible value of the S wave magnitude and phase relative to δ_P^1 but it is in such violent disagreement with unitarity (except right at the P-wave resonance) that there can be no question that it is unphysical. In addition, it is of course impossible, as in any energy independent phase shift analysis, to rule out rapid 180^o changes in the phase shifts between any two neighboring mass bins.

4.4 $K^-\pi^+$ and $K^+\pi^-$ Partial Waves in the Inelastic Region

In mass regions where the $K\pi$ partial waves may be inelastic, it is no longer sensible to impose elastic unitarity. Without accurate information on the total cross section or on inelastic channels, the data determine only the magnitudes and relative phases of the different partial waves. Fortunately, in nonexotic channels such as $K^-\pi^+$ or $K^+\pi^-$, the existence of resonances in the leading partial waves, coupled with unitarity and continuity requirements, provides strong constraints on this phase. There is also a problem of discrete ambiguities* in the inelastic region. This is most readily apparent as an indeterminacy in the signs of the imaginary parts of the (Barrelet) zeros [16], z_i, of the scattering amplitude and, in fact, the signs of Im z_i provide a convenient [17] means of distinguishing and classifying the various solutions for

*We truncate the partial wave expansions at L=3. Small nonzero higher partial waves lead to the usual continuum ambiguity patches around our solutions.

the partial waves. Moreover, only when one of the Im z_i approaches zero is it possible to change from one solution to another. In the $K\pi$ case, since elastic unitarity allows only one solution up to about 1.3 GeV, the possibility of discrete ambiguities does not arise until one of the Im z_i approaches zero. From Fig. 9 where the real and imaginary parts of the zeros have been plotted (for one choice of sign for Im z_i), it is apparent that this cannot occur before $M_{K\pi} \sim 1.45$ GeV. However, in the region from 1.4 to 1.5 GeV, both Im z_1 and Im z_2 could change sign so that although below 1.4 GeV there is only one possible solution, above 1.5 GeV there are four which can be specified by the signs of Im z_1 and Im z_2, as indicated in Table 2.*

In Figs. 10 and 11 we present the magnitudes and phases of the $K^-\pi^+$ and $K^+\pi^-$ partial waves for all four solutions. Although the solution is unique for $M_{K\pi} < 1.5$ GeV, for clarity we show each solution in the mass interval 1.3 to 1.9 GeV, and include the magnitudes and phases for the full mass range with solution A. The S and P partial waves below 1.3 GeV were calculated from the I=1/2 and I=3/2 phase shifts shown in Figs. 7 and 8. In this $M_{K\pi}$ region the imposition of elastic unitarity determines the overall phase. Above 1.3 GeV, the data determine only the relative phases of the different partial waves. For $1.3 < M_{K\pi} < 1.6$ GeV, the S, P and F wave phases are shown relative to the (absolute) D wave Breit-Wigner phase. This was obtained by fitting the D wave magnitudes from 1.25 to 1.6 GeV to a Breit-Wigner form (curves on Figs. 10 and 11), yielding resonance parameters listed in Table 1d where, once again, the good agreement between neutron and delta recoil reactions is evident. Above 1.6 GeV the phases are measured relative to ϕ_F. For plotting purposes,

*We have chosen to label the $K\pi$ solutions in the same way as the $\pi\pi$ solutions of ref. [17].

the F wave phase has been chosen to correspond to that of a resonance [4] of mass 1.78 GeV and width of 175 MeV. We emphasize that at each mass value the choice of overall phase is arbitrary and all values provide identical values of $d\sigma_{K\pi}/d\Omega$.

4.5 Simultaneous Neutron/Delta Analyses

The results of the previous subsections indicate good agreement between $K\pi$ partial waves calculated from the neutron recoil reactions (1) and (2) and those obtained using the delta recoil reactions (3) and (4). Moreover, it is straightforward to apply the analysis techniques of section 4.1 to a combined neutron/delta analysis. As before, we express the $K\pi$ moments in terms of the partial wave amplitudes and the t averages $<L'_\lambda L^*_\mu>$ of Eq. (13). Now, however, the a_L are common to the neutron and delta recoil reactions while the $<L'_\lambda L^*_\mu>$ are calculated separately for each reaction.

The I=3/2 S wave phase shifts obtained from the combined $K^+\pi^+/K^-\pi^-$ analysis are plotted in Fig. 12a. As before, we find that the I=3/2 P and D waves are negligible (always less than 3^o) and that the $M_{K\pi}$ dependence of δ_S^3 is well described by the effective range formula of Eq. (14) with the parameters listed in Table 1a. This fit is represented by the curve on Fig. 12a and also serves to specify the δ_S^3 input in the elastic $K^+\pi^-/K^-\pi^+$ analysis.

The I=1/2 S and P wave phase shifts obtained from the joint $K^+\pi^-/K^-\pi^+$ analysis are shown in Fig. 12b for $M_{K\pi} < 1.3$ GeV. Once again, we see a steady increase with $M_{K\pi}$ of $\delta_S^{1/2}$, which is well described by an effective range form with the parameters of Table 1c. Apart from the single $M_{K\pi}$ bin at 895 MeV, we find no evidence for the up solution for δ_S^1. It is, of course, not possible to rule out sudden 180^o changes in any phase shift. The K*(890) resonance

parameters resulting from a Breit-Wigner fit to δ_p^1 for $0.8 < M_{K\pi} < 1.0$ GeV are listed in Table 1b.

In the inelastic region, $M_{K\pi} > 1.3$ GeV, there is still not a unique solution for the partial wave magnitudes and relative phases for $K\pi$ masses above 1.48 GeV. We therefore present, in Fig. 13 and Table 3, all four possible solutions for the $K\pi$ partial waves for $M_{K\pi} > 1.48$ GeV, as well as the unique solution for lower masses. As before, we choose the overall phase in the region $1.3 < M_{K\pi} < 1.6$ GeV so that ϕ_D corresponds to a D wave Breit-Wigner, the parameters of which are obtained by fitting the D wave magnitude to a Breit-Wigner form in the region $1.25 < M_{K\pi} < 1.60$ GeV. These parameters are listed in Table 1d. For plotting purposes for $M_{K\pi} > 1.6$ GeV, ϕ_F is chosen to have the phase associated with a resonance of mass 1780 MeV and width 175 MeV [1], as shown by the curves in Fig. 13. Taking these values for the mass and width of the 3^- resonance, we calculate an elasticity of $(19 \pm 2)\%$. We emphasize once again that for each value of $M_{K\pi}$ the choice of overall phase is arbitrary.

A comparison of all the partial wave results presented in Figs. 7, 8, 10, 11, 12, and 13 and the results listed in Table 1 illustrates the consistency of the separate $K^-\pi^+$, $K^+\pi^-$, and combined analyses. We also found that the magnitude of χ^2 obtained from the individual fits to determine the partial waves at each $K\pi$ mass was similar for the separate neutron recoil and delta recoil analyses, and that in the combined analysis fits the contribution to χ^2 from the two different input data sets was comparable. It should also be pointed out that at high $K\pi$ mass the statistics of the neutron and delta recoil data are similar.

Figure 13 shows not only the presence of resonances in the leading 1^-, 2^+ and 3^- partial waves but also interesting structure in some of the nonleading

partial wave amplitudes. For instance, in solutions B and D there is a bump in $|a_p|$, coupled with a fairly rapid increase of ϕ_p, in the 1.6 to 1.8 GeV region. Furthermore, in all four solutions, there is a rapid decrease in $|a_s|$ just above 1.4 GeV. This effect is more obvious in Fig. 14 where we compare the S wave magnitude and phase of solution B with the extrapolation (dashed line) of the effective range fits. Figure 14 also compares the P wave magnitude and phase with the extrapolation to higher masses of the K*(890) Breit-Wigner fits. These effects and their interpretation will be discussed at greater length in the next section.

5. Discussion of Results

Before discussing the new features of $K\pi$ scattering resulting from our analysis, we first compare our results with those of other experiments. In subsection 5.1 we discuss the I=3/2 $K\pi$ scattering results, in 5.2 we compare results for I=1/2 $K\pi$ scattering in the elastic region, and in 5.3 we discuss briefly the spin-parity 2^+ K*(1435) resonance. In 5.4, we present Argand diagrams for the four possible $K\pi$ solutions and discuss their structure in terms of resonances in the nonleading partial waves. We find evidence for a new I=1/2 S wave resonance and also, in two of the solutions, for a new 1^- $K\pi$ resonance. In subsection 5.5, we compare $K\pi$ and $\pi\pi$ scattering and in 5.6 we discuss possible methods for solving the ambiguity problem.

5.1 I=3/2 $K\pi$ Scattering

We have already remarked that charge two $K\pi$ scattering is dominated by the S wave, with δ_P^3 and δ_D^3 always less than three degrees. The I=3/2 S wave phase shift, δ_S^3, is well described by an effective range form and corresponds to a total cross section decreasing from 4 mb at 0.9 GeV to 2 mb at 1.5 GeV.

This calculation depends on the assumption that the S wave is elastic. If some inelasticity were allowed, the cross section would be larger.

Our phase shifts are somewhat larger but, in general, consistent with previous measurements [7]. These previous measurements, which individually have large statistical and systematic uncertainties, are usually collectively represented as corresponding to a constant total cross section of 1.8 mb. Since our I=3/2 normalization is extremely well known from (i) the existence of the elastic P wave K*(890) resonance and (ii) the directly measured relative K^+/K^- experimental normalization, our results should be much more reliable.

5.2 Kπ Scattering in the Elastic Region

Our results for the I=1/2 S wave phase shift, δ_s^1, in the elastic region ($M_{K\pi} < 1.3$ GeV) are in good agreement with, but of much higher statistical significance than, other [8, 18] experimental results. We note that our determination of the neutral K*(890) mass and width agrees with the currently accepted values quoted in ref. [15]. It is amusing to note that our value of $a_s^1/a_s^3 \simeq -2.4$ agrees with the current algebra prediction [19] of -2, although each individual scattering length is approximately twice as large as expected from current algebra. Scattering length comparisons are complicated by (i) the difficulty of extracting the π exchange signal from the large background in reactions (1) to (4) in the threshold region below 800 MeV, and (ii) by the large current algebra predictions for the effective range parameters, r_s.

5.3 The K*(1435) Resonance

In contrast with the good agreement of our phase shifts with other results, our best estimate of the mass of the neutral 2^+ resonance is some 15 MeV higher than the Particle Data Group [20]. This effect, which is also noted in another recent Kπ analysis [18], can be attributed to the fact that most previous

determinations of the K*(1420) mass came from fits to $K\pi$ mass spectra in which the background was parametrized as a low-order polynomial. It is apparent from Fig. 13 that for $M_{K\pi} < 1.4$ GeV, the S wave is at least as large a contribution to the $K\pi$ cross section as the D wave is, and is a slowly varying function of $M_{K\pi}$. However, the rapid decrease (in all four solutions) of $|a_s|$ just above 1.4 GeV results in a cross section which peaks at a $K\pi$ mass below the D wave resonance. We conclude that our result, 1434 ± 2 MeV, based on fits to the extracted D wave amplitude, yields a more reliable measurement of the resonance parameter values; it follows that the $J^P=2^+$ $K\pi$ resonance should more properly be designated the K*(1435).

5.4 Argand Diagrams and Nonleading Resonances

The $K\pi$ partial wave results of the preceding section, as well as demonstrating the existence of the leading 1^-, 2^+ and 3^- resonances, exhibit interesting new structure in the 0^+ wave and also, for solutions B and D, in the P wave. These effects are perhaps more readily apparent in the Argand diagrams of Fig. 15. The points for $M_{K\pi} > 1.48$ GeV shown in Fig. 15 were obtained from a joint partial wave analysis of the $K^+\pi^-$ and $K^-\pi^+$ data in overlapping 120 MeV bins at 40 MeV intervals. The results of this overlapping bin analysis are given in Table 4. In each $M_{K\pi}$ interval above 1.3 GeV, the overall phase was chosen by requiring approximate Breit-Wigner behavior of the leading partial waves as well as satisfying unitarity and continuity. The amount of rotation from the initial Breit-Wigner phases is listed in Tables 3 and 4. The I=1/2 S wave was calculated by subtracting from the full $K^+\pi^-/K^-\pi^+$ S wave the elastic I=3/2 contribution given by the effective range fits shown in Fig. 12.

Figure 15 clearly shows the circular motion of the S wave in the Argand diagrams for all four solutions. Moreover, in all solutions, the speed is

greatest in the region of 1.4 to 1.5 GeV. Although the distance between adjacent points on the Argand diagrams is obviously very sensitive to the choice of overall phase at each point, it seems extremely likely that almost all reasonable phase choices will exhibit resonant S wave behavior similar to that of Fig. 15. We therefore conclude that, in all four solutions, there is an S wave resonance with a mass of 1.4 to 1.45 GeV, width of 200-300 MeV, and branching ratio to $K\pi$ of about 0.8, 0.9, 0.5 or 0.8 for solution A, B, C or D, respectively as listed in Table 5. Historically, the 0^+ κ meson has been associated with the point where δ_S^1 finally reaches 90^o. We find that this point occurs at a mass of about 1.35 GeV. It is difficult to quote a width for this so-called resonance due to the existence of the relatively narrow 0^+ resonance above 1400 MeV. The 'width' calculated from the 45^o point at 900 MeV would be about 900 MeV.

Figure 15 also shows, in solutions B and D, a resonance-like circular motion of the 1^- partial wave. As we have just discussed with reference to the S wave, the details of this behavior, in particular the speed, are sensitive to the choice of overall phase. We estimate that this effect could be due to a P wave resonance with a mass of 1.65 GeV, width of 250-300 MeV, and branching ratio to $K\pi$ of 25 to 30%. In view of the present lack of understanding of the problems of resonance definition and the determination of resonance pole parameters, we eschew a more quantitative determination of these S and P wave resonance parameters.

An additional way of displaying the structure in these partial waves is shown in Fig. 16 where for solution B we have plotted the projections of the real and imaginary parts of the partial wave amplitudes along with their Argand diagrams normalized to unitarity circles of unit diameter. It is important, when attempting to infer resonance behavior from these plots, to remember

that nonresonant backgrounds can severely affect the mass dependence of the partial waves.

5.5 Comparison of $K\pi$ and $\pi\pi$ Scattering

The similarity between the $K\pi$ partial waves of Fig. 15 and the $\pi\pi$ partial waves (see, for example, Fig. 6 of ref. [17]) is truly remarkable:

- both $K\pi$ and $\pi\pi$ systems have leading P, D and F wave resonances
- both systems show evidence of S wave resonance behavior in the region of the leading D wave resonances
- both systems indicate a P wave resonance in the region of the leading (highly inelastic) F wave state for solutions B and D
- both systems have large S wave backgrounds in both exotic and nonexotic charge states, while little (nonresonant) background is present in the $L > 0$ partial waves.

It is indeed pleasing that the detailed dynamical behavior of the $K\pi$ and $\pi\pi$ systems is so consistent with the naivest considerations of symmetry ideas.

5.6 Resolution of Ambiguities

It is important to determine which of the $K\pi$ partial wave solutions is the physical one. Unfortunately, as discussed in section 4, all four solutions give rise to the same $K\pi$ differential cross section. Moreover, none of the four solutions strongly violates unitarity. We also expect that, as in the $\pi^+\pi^-$ case, analyticity in the form of fixed u dispersion relations will severely constrain the overall phase but not rule out any of the possible solutions. Data on inelastic channels could help to rule out solutions. For instance, observation of a large P wave cross section (of the order of 1.5 mb) in $K\pi\pi$ or some other inelastic channel in the mass region around 1.6 GeV would eliminate solutions A and C from the realm of possibilities. On the other hand, nonobservation of

such a large P wave cross section would only be useful in resolving the ambiguity if all inelastic channels had been observed. Even if such considerations do not distinguish between solutions, they will certainly provide strong constraints on the overall phase.

Another possible way of resolving the ambiguities would be to measure the $K^0\pi^0$ final state produced via π exchange. These states have relative I=1/2 and I=3/2 couplings which are different from those in $K^{\pm}\pi^{\mp}$. Figure 16 shows the predictions of each of the four $K\pi$ solutions for the differential cross section and unnormalized M=0, $L\leq 3$ moments for the reaction $K^-p \rightarrow \overline{K}^0\pi^0 n$ at 13 GeV/c with $|t'| < 0.15$ GeV^2. We illustrate the sensitivity of the $K^0\pi^0$ predictions to the choice of overall phase by plotting bands of values corresponding to variations of $\pm 10^0$ from the phases as plotted in Fig. 15. It is apparent from Fig. 16 that an accurate measurement of $K^0\pi^0$ production for $1.4 < M_{K\pi} < 2$ GeV could distinguish between solutions.

One might also hope that, in view of the striking similarity between the $\pi\pi$ and $K\pi$ partial waves, resolution of the ambiguity problem in $\pi\pi$, for instance by measurements of $\pi^0\pi^0$ production, would, via SU(3), also resolve the $K\pi$ ambiguity.

6. Summary and Conclusions

Data on reactions (1) to (4) have allowed us to calculate the $K\pi$ partial waves for both the neutral and doubly charged $K\pi$ systems. The observed agreement between the $K\pi$ partial waves calculated using only the neutron recoil reactions (1) and (2) and those calculated using only the Δ^{++} recoil reactions (3) and (4) indicates not only that the relative experimental K^+/K^- normalization is correct but also that we understand the production mechanisms at least well enough to extract the physical $K\pi$ scattering amplitudes. A joint

analysis of neutron and Δ^{++} recoil reactions clearly provides the best estimate of the $K\pi$ partial waves. We find evidence for a $J^P=0^+$ resonance at 1425 MeV with a width of about 250 MeV and a $K\pi$ branching fraction of between 0.5 and 0.9, depending upon the solution. This reopens the question of the status of the 0^+ nonet. We also find, in two solutions, evidence for a 1^- resonance at about 1650 MeV; this is presumably the SU(3) partner of the $\rho'(1600)$. Accurate measurements of $K^o\pi^o$ production for $K\pi$ mass between 1.4 and 2.0 GeV should make it possible to establish which of the four possible partial wave solutions is the physical one.

References

[1] W. M. Dunwoodie et al., to be published.

[2] P. Estabrooks et al., Phys. Lett. 60B (1976) 473.

[3] P. Estabrooks et al., Nucl. Phys. B106 (1976) 61.

[4] G. Brandenburg et al., Phys. Lett. 60B (1976) 478.

[5] G. Brandenburg et al., to be published.

[6] G. Brandenburg et al., Phys. Lett. 59B (1975) 405.

[7] D. Linglin et al., Nucl. Phys. B57 (1973) 64.
A. M. Bakker et al., Nucl. Phys. B24 (1970) 211.

[8] M. J. Matison et al., Phys. Rev. D 9 (1974) 1872.
H. H. Bingham et al., Nucl. Phys. B41 (1972) 1.
R. Mercer et al., Nucl. Phys. B32 (1971) 381.

[9] A. B. Wicklund et al., Argonne National Laboratory report; contributed paper to the XVII Int. Conf. on High Energy Physics, London, 1974.

[10] P. Estabrooks and A. D. Martin, Nucl. Phys. B102 (1976) 537.

[11] A. D. Martin and C. Michael, Nucl. Phys. B84 (1975) 83.

[12] C. Goebel, Phys. Rev. Lett. 1 (1958) 337.
G. F. Chew and F. Low, Phys. Rev. 113 (1959) 1640.

[13] L. Stodolsky and J. J. Sakurai, Phys. Rev. Lett. 11 (1963) 90.

[14] G. Grayer et al., Nucl. Phys. B75 (1974) 189.

[15] Particle Data Group, Rev. Mod. Phys. 48 (1976) 51.

[16] E. Barrelet, Nuovo Cimento 8A (1972) 331.

[17] P. Estabrooks and A. D. Martin, Nucl. Phys. B95 (1975) 322.

[18] M. G. Bowler et al., Oxford University preprint Ref. 4/77 (1977).

[19] See, for example, J. L. Petersen, Phys. Rep. 2C (1971) 155.

Table 1

The values of the parameters describing the $M_{K\pi}$ dependence of (a) the I = 3/2 S wave, (b) the I = 1/2 P wave for $0.8 < M_{K\pi} < 1$ GeV, (c) the I = 1/2 S wave for $M_{K\pi} < 1.2$ GeV and (d) the D wave magnitude in the mass range $1.25 < M_{K\pi} < 1.6$ GeV. The errors reflect the systematic, as well as the statistical, uncertainties.

Parameter	Neutron Recoil Only	Δ^{++} Recoil Only	Combined Analysis
(a) $a_s^3(\text{GeV}^{-1})$	-1.03 ± 0.10	-0.92 ± 0.08	-1.00 ± 0.05
$r_s^3(\text{GeV}^{-1})$	-0.94 ± 0.5	-1.30 ± 0.4	-1.76 ± 0.3
(b) M_R(MeV)	896.0 ± 0.7	895.3 ± 0.3	895.7 ± 0.3
Γ(MeV)	50.5 ± 1.1	52.5 ± 0.4	52.9 ± 0.4
$R(\text{GeV}^{-1})$	6.9 ± 2.7	3.7 ± 0.5	4.3 ± 0.4
(c) $a_s^1(\text{GeV}^{-1})$	2.4 ± 0.1	2.28 ± 0.05	2.39 ± 0.04
$r_s^1(\text{GeV}^{-1})$	-1.7 ± 0.3	-2.2 ± 0.1	-1.76 ± 0.10
(d) x	0.51 ± 0.03	0.48 ± 0.03	0.49 ± 0.02
M_R(MeV)	1431 ± 5	1439 ± 4	1434 ± 2
Γ(MeV)	88 ± 9	109 ± 8	98 ± 5
$R(\text{GeV}^{-1})$	2.0 ± 0.9	3.3 ± 1.0	2.4 ± 0.6

Table 2

The definition of the four possible $K^-\pi^+$ partial wave solutions according to the signs of the Im z_i at $M_{K\pi} = 1.6$ GeV. The existence of the K*(1435) resonance requires Im $z_2 < 0$ below about 1.5 GeV and the K*(1780) resonance requires Im $z_3 < 0$ everywhere.

Solution	Im $z_1(1.6)$	Im $z_2(1.6)$
A	-	-
B	+	-
C	-	+
D	+	+

Table 3

The Kπ partial waves of Fig. 12 and 13, as calculated from the joint fits to the neutron and delta recoil reactions.

(a) The I = 3/2 S, P, and D wave phase shifts.

$M_{K\pi}$	δ_S^3	δ_P^3	δ_D^3	$M_{K\pi}$	δ_S^3	δ_P^3	δ_D^3
0.73	-10.0 ± 0.5			1.22	-23.5 ± 0.6	-0.6 ± 0.3	-1.5 ± 0.2
0.82	-14.5 ± 1.5			1.26	-23.9 ± 0.7	-0.6 ± 0.3	-1.3 ± 0.3
0.90	-16.5 ± 1.5			1.30	-23.8 ± 0.7	-0.1 ± 0.4	-1.7 ± 0.3
0.94	-17.0 ± 0.6			1.34	-26.4 ± 0.7	-0.7 ± 0.4	-2.5 ± 0.3
0.98	-18.0 ± 1.2			1.38	-25.0 ± 0.9	-0.3 ± 0.4	-1.5 ± 0.4
1.02	-18.5 ± 1.0	-0.8 ± 0.2	-0.7 ± 0.2	1.44	-27.4 ± 0.6	-1.2 ± 0.3	-2.3 ± 0.3
1.06	-18.2 ± 0.7	-0.2 ± 0.3	-0.6 ± 0.2	1.52	-26.7 ± 0.7	-2.4 ± 0.3	-1.5 ± 0.3
1.10	-21.4 ± 0.5	-0.9 ± 0.3	-1.3 ± 0.2	1.60	-25.6 ± 1.0	-2.1 ± 0.4	-1.4 ± 0.4
1.14	-21.1 ± 0.5	-1.1 ± 0.3	-1.2 ± 0.2	1.72	-22.8 ± 1.0	-2.4 ± 0.4	-0.5 ± 0.2
1.18	-22.4 ± 0.5	-0.6 ± 0.3	-1.3 ± 0.2				

(b) The I = 1/2 S and P wave phase shifts in the elastic region.

$M_{K\pi}$	δ_S^1	δ_P^1	$M_{K\pi}$	δ_S^1	δ_P^1	$M_{K\pi}$	δ_S^1	δ_P^1
0.730	21.0 ± 3.0	6.0 ± 0.9	0.895	39.6 ± 1.5	96.2 ± 3.1	1.020	53.9 ± 0.8	162.9 ± 0.4
0.780	27.2 ± 2.8	10.0 ± 0.7	0.905	34.7 ± 1.3	108.3 ± 1.3	1.060	57.8 ± 0.8	165.2 ± 0.4
0.820	40.7 ± 0.9	14.0 ± 0.5	0.915	33.5 ± 1.7	122.4 ± 0.8	1.100	60.2 ± 0.9	167.5 ± 0.5
0.845	36.8 ± 1.4	23.9 ± 0.5	0.925	37.2 ± 1.8	134.6 ± 0.7	1.140	61.2 ± 0.9	168.5 ± 0.6
0.855	40.4 ± 1.6	28.3 ± 0.5	0.935	40.9 ± 1.7	140.4 ± 0.6	1.180	66.3 ± 2.0	173.0 ± 1.8
0.865	38.0 ± 2.3	39.5 ± 0.5	0.945	42.8 ± 1.7	147.4 ± 0.6	1.220	69.3 ± 1.4	170.8 ± 1.6
0.875	38.1 ± 1.1	49.6 ± 0.6	0.955	46.9 ± 1.6	150.9 ± 0.7	1.260	71.7 ± 4.8	166.7 ± 4.2
0.885	39.1 ± 1.2	70.6 ± 1.1	0.980	48.4 ± 0.7	157.0 ± 0.3	1.300	79.3 ± 1.8	176.3 ± 8.8

Table 3, continued

(c) Kπ partial waves in the inelastic region. All four solutions are identical below $M_{K\pi}$ = 1.5 (column is the phase rotation, θ_{rot}, required to give the overall phase shown in Fig. 15. Not $1.28 < M_{K\pi} < 1.60$ the D wave is chosen as the reference wave and that in the region $M_{K\pi} > 1.($ is chosen as the reference wave.

Solution A

$M_{K\pi}$	θ_{rot}	$\lvert a_S \rvert$	ϕ_S	$\lvert a_P \rvert$	ϕ_P	$\lvert a_D \rvert$	ϕ_D	$\lvert a_F \rvert$
1.14	0.	0.87 ± 0.01	73. ± 1.	0.35 ± 0.02	169. ± 1.	0.01 ± 0.02	0. ± 1.	
1.18	0.	0.93 ± 0.01	78. ± 2.	0.21 ± 0.05	173. ± 2.	0.09 ± 0.09	5. ± 1.	
1.22	0.	0.96 ± 0.01	81. ± 1.	0.28 ± 0.05	171. ± 2.	0.04 ± 0.06	2. ± 2.	
1.26	0.	0.98 ± 0.03	83. ± 5.	0.40 ± 0.12	157. ± 4.	0.01 ± 0.14	1. ± 6.	
1.30	-6.	1.01 ± 0.02	99. ± 2.	0.13 ± 0.03	157. ± 9.	0.35 ± 0.02	14.	
1.34	-6.	1.05 ± 0.02	104. ± 3.	0.20 ± 0.05	164. ±10.	0.40 ± 0.04	22.	
1.38	-3.	1.06 ± 0.02	109. ± 2.	0.19 ± 0.03	154. ± 8.	0.75 ± 0.03	39.	
1.42	-7.	1.00 ± 0.01	126. ± 1.	0.20 ± 0.02	163. ± 7.	1.02 ± 0.02	74.	
1.46	-10.	0.84 ± 0.01	142. ± 1.	0.21 ± 0.01	169. ± 8.	1.02 ± 0.02	115.	
1.50	-6.	0.52 ± 0.03	146. ± 2.	0.30 ± 0.07	209. ± 7.	0.71 ± 0.02	138.	0.08 ± 0.
1.56	-11.	0.40 ± 0.02	164. ± 3.	0.32 ± 0.05	222. ± 5.	0.58 ± 0.02	152.	0.12 ± 0.
1.65	13.	0.33 ± 0.02	143. ± 8.	0.22 ± 0.03	177. ±17.	0.48 ± 0.02	135. ± 7.	0.29 ± 0.
1.75	2.	0.39 ± 0.02	131. ± 4.	0.23 ± 0.02	160. ±11.	0.44 ± 0.02	148. ± 4.	0.43 ± 0.
1.85	-18.	0.48 ± 0.03	153. ± 6.	0.28 ± 0.04	189. ±10.	0.48 ± 0.02	183. ± 7.	0.43 ± 0.

Solution B

$M_{K\pi}$	θ_{rot}	$\lvert a_S \rvert$	ϕ_S	$\lvert a_P \rvert$	ϕ_P	$\lvert a_D \rvert$	ϕ_D	$\lvert a_F \rvert$
1.50	-16.	0.63 ± 0.01	161. ± 2.	0.16 ± 0.07	103. ±18.	0.58 ± 0.03	138.	0.09 ± 0.
1.56	-16.	0.56 ± 0.01	183. ± 3.	0.22 ± 0.05	114. ±11.	0.50 ± 0.04	152.	0.11 ± 0.
1.65	-6.	0.27 ± 0.03	190. ±10.	0.50 ± 0.02	111. ± 8.	0.30 ± 0.02	141. ±10.	0.28 ± 0.
1.75	0.	0.14 ± 0.04	97. ± 7.	0.53 ± 0.02	144. ± 4.	0.23 ± 0.02	138. ± 8.	0.43 ± 0.
1.85	-27.	0.36 ± 0.03	122. ±10.	0.52 ± 0.03	187. ± 8.	0.33 ± 0.03	165. ± 7.	0.43 ± 0

ϕ_S	$\lvert a_P \rvert$	ϕ_P	$\lvert a_D \rvert$	ϕ_D	$\lvert a_F \rvert$
114. ± 1.	0.17 ± 0.07	75. ±18.	0.67 ± 0.03	138.	0.09 ± 0.
122. ± 2.	0.20 ± 0.05	83. ±10.	0.48 ± 0.04	152.	0.12 ± 0.
117. ± 6.	0.20 ± 0.03	98. ±16.	0.31 ± 0.02	141. ± 8.	0.28 ± 0.
127. ± 3.	0.23 ± 0.02	119. ± 9.	0.29 ± 0.01	139. ± 6.	0.41 ± 0.
152. ± 3.	0.30 ± 0.04	115. ± 8.	0.29 ± 0.02	149. ± 8.	0.43 ± 0.

Table 3, continued

Solution C

$M_{K\pi}$	θ_{rot}	$\lvert a_S \rvert$	ϕ_S	$\lvert a_P \rvert$	ϕ_P	$\lvert a_D \rvert$	ϕ_D	$\lvert a_F \rvert$	ϕ_F	σ_{tot}(mb)
1.50	12.	0.64 ± 0.01	114. ± 1.	0.17 ± 0.07	75. ±18.	0.67 ± 0.03	138.	0.09 ± 0.04	7. ± 23.	18
1.56	-3.	0.59 ± 0.01	122. ± 2.	0.20 ± 0.05	83. ±10.	0.48 ± 0.04	152.	0.12 ± 0.03	29. ± 12.	16
1.65	8.	0.55 ± 0.02	117. ± 6.	0.20 ± 0.03	98. ±16.	0.31 ± 0.02	141. ± 8.	0.28 ± 0.03	30.	14
1.75	10.	0.56 ± 0.02	127. ± 3.	0.23 ± 0.02	119. ± 9.	0.29 ± 0.01	139. ± 6.	0.41 ± 0.02	70.	16
1.85	-12.	0.61 ± 0.02	152. ± 3.	0.30 ± 0.04	115. ± 8.	0.29 ± 0.02	149. ± 8.	0.43 ± 0.03	127.	16

Solution D

$M_{K\pi}$	θ_{rot}	$\lvert a_S \rvert$	ϕ_S	$\lvert a_P \rvert$	ϕ_P	$\lvert a_D \rvert$	ϕ_D	$\lvert a_F \rvert$	ϕ_F	σ_{tot}(mb)
1.50	18.	0.45 ± 0.03	127. ± 4.	0.49 ± 0.06	58. ± 9.	0.64 ± 0.03	138	0.08 ± 0.04	2. ± 24.	20
1.56	10.	0.24 ± 0.03	121. ±10.	0.60 ± 0.04	70. ± 5.	0.42 ± 0.04	152.	0.11 ± 0.03	17 ± 23.	17
1.65	13.	0.23 ± 0.03	92. ±13.	0.55 ± 0.02	99. ± 7.	0.12 ± 0.05	174. ±12.	0.31 ± 0.03	30.	15
1.75	9.	0.38 ± 0.03	91. ± 3.	0.51 ± 0.02	132. ± 4.	0.13 ± 0.02	90. ±11.	0.42 ± 0.02	70.	18
1.85	-8.	0.58 ± 0.03	123. ± 5.	0.36 ± 0.03	159. ± 8.	0.27 ± 0.03	113. ± 7.	0.42 ± 0.03	127.	16

Table 4

The Kπ partial waves in the mass region above 1.48 GeV, as calculated from the joint fits to the neutron and delta recoil reactions using data in overlapping 120 MeV bins. Note that for $1.28 < M_{K\pi} < 1.60$ the D wave is chosen as the reference wave and that in the region $M_{K\pi} > 1.6$ GeV, the F wave is chosen as the reference wave.

Solution A

$M_{K\pi}$	θ_{rot}	$\lvert a_S \rvert$	ϕ_S	$\lvert a_P \rvert$	ϕ_P	$\lvert a_D \rvert$	ϕ_D	$\lvert a_F \rvert$	ϕ_F
1.50	- 6	0.57 ± 0.01	149 ± 2	0.30 ± 0.04	210 ± 4	0.82 ± 0.01	138	0.12 ± 0.03	31 ± 6
1.54	-10	0.49 ± 0.02	155 ± 2	0.20 ± 0.03	205 ± 7	0.62 ± 0.01	148	0.16 ± 0.03	43 ± 5
1.58	-10	0.40 ± 0.03	159 ± 4	0.23 ± 0.04	213 ± 8	0.46 ± 0.02	154	0.21 ± 0.03	35 ± 6
1.62	17	0.36 ± 0.01	134 ± 6	0.19 ± 0.01	151 ± 17	0.51 ± 0.01	124 ± 5	0.29 ± 0.03	24
1.66	12	0.30 ± 0.02	148 ± 7	0.22 ± 0.02	180 ± 14	0.45 ± 0.02	139 ± 6	0.31 ± 0.02	32
1.70	11	0.33 ± 0.02	130 ± 5	0.23 ± 0.01	155 ± 12	0.48 ± 0.01	133 ± 4	0.37 ± 0.02	45
1.74	5	0.40 ± 0.02	130 ± 3	0.25 ± 0.02	157 ± 9	0.43 ± 0.02	144 ± 4	0.42 ± 0.02	65
1.78	- 8	0.40 ± 0.02	139 ± 2	0.24 ± 0.02	168 ± 7	0.43 ± 0.02	162 ± 4	0.45 ± 0.02	90
1.82	-15	0.46 ± 0.03	148 ± 2	0.23 ± 0.03	173 ± 8	0.40 ± 0.02	174 ± 6	0.46 ± 0.02	113
1.86	-18	0.48 ± 0.03	151 ± 4	0.22 ± 0.03	167 ± 11	0.38 ± 0.02	178 ± 5	0.46 ± 0.03	130

Solution B

$M_{K\pi}$	θ_{rot}	$\lvert a_S \rvert$	ϕ_S	$\lvert a_P \rvert$	ϕ_P	$\lvert a_D \rvert$	ϕ_D	$\lvert a_F \rvert$	ϕ_F
1.50	-16	0.69 ± 0.01	164 ± 2	0.17 ± 0.06	103 ± 15	0.77 ± 0.02	138	0.12 ± 0.03	30 ± 10
1.54	-19	0.53 ± 0.02	172 ± 2	0.34 ± 0.03	93 ± 4	0.50 ± 0.03	148	0.16 ± 0.03	38 ± 7
1.58	-13	0.35 ± 0.03	176 ± 5	0.45 ± 0.02	98 ± 4	0.30 ± 0.02	154	0.21 ± 0.03	16 ± 8
1.62	- 3	0.29 ± 0.02	170 ±10	0.48 ± 0.02	94 ± 7	0.31 ± 0.02	131 ± 7	0.29 ± 0.03	24
1.66	- 6	0.22 ± 0.02	191 ±11	0.45 ± 0.03	116 ± 7	0.29 ± 0.02	140 ± 7	0.33 ± 0.02	32
1.70	6	0.10 ± 0.04	169 ±20	0.55 ± 0.02	121 ± 5	0.25 ± 0.02	131 ± 7	0.37 ± 0.02	45
1.74	0	0.15 ± 0.03	104 ± 7	0.55 ± 0.02	140 ± 4	0.24 ± 0.02	135 ± 7	0.42 ± 0.02	65
1.78	- 8	0.21 ± 0.03	101 ±10	0.53 ± 0.02	159 ± 3	0.24 ± 0.02	147 ± 6	0.45 ± 0.02	90
1.82	-19	0.34 ± 0.03	116 ± 3	0.48 ± 0.02	176 ± 4	0.25 ± 0.03	154 ± 5	0.46 ± 0.02	113
1.86	-28	0.33 ± 0.04	121 ± 5	0.46 ± 0.03	195 ± 6	0.31 ± 0.02	169 ± 8	0.41 ± 0.03	130

Table 4, continued

Solution C

$M_{K\pi}$	θ_{rot}	$\lvert a_S \rvert$	ϕ_S	$\lvert a_P \rvert$	ϕ_P	$\lvert a_D \rvert$	ϕ_D	$\lvert a_F \rvert$	ϕ_F
1.50	12	0.69 ± 0.01	110 ± 1	0.22 ± 0.06	64 ± 9	0.76 ± 0.02	138	0.07 ± 0.04	13 ± 20
1.54	2	0.59 ± 0.01	122 ± 1	0.26 ± 0.04	72 ± 4	0.51 ± 0.03	148	0.14 ± 0.03	35 ± 7
1.58	- 7	0.56 ± 0.01	132 ± 3	0.13 ± 0.01	129 ± 15	0.39 ± 0.01	154	0.15 ± 0.02	22 ± 9
1.62	12	0.54 ± 0.01	111 ± 5	0.25 ± 0.04	75 ± 10	0.30 ± 0.02	135 ± 7	0.26 ± 0.03	24
1.66	7	0.53 ± 0.01	120 ± 4	0.19 ± 0.02	106 ± 12	0.28 ± 0.02	144 ± 7	0.30 ± 0.02	32
1.70	16	0.56 ± 0.01	116 ± 3	0.23 ± 0.02	99 ± 8	0.27 ± 0.01	130 ± 6	0.35 ± 0.02	45
1.74	10	0.56 ± 0.02	124 ± 2	0.24 ± 0.02	122 ± 8	0.31 ± 0.01	135 ± 4	0.41 ± 0.02	65
1.78	2	0.53 ± 0.02	140 ± 2	0.22 ± 0.02	136 ± 7	0.30 ± 0.01	153 ± 4	0.44 ± 0.02	90
1.82	-13	0.59 ± 0.02	149 ± 2	0.24 ± 0.03	136 ± 8	0.29 ± 0.01	157 ± 6	0.44 ± 0.02	113
1.86	-13	0.58 ± 0.02	156 ± 3	0.24 ± 0.04	122 ± 7	0.27 ± 0.02	144 ± 7	0.40 ± 0.03	130

Solution D

$M_{K\pi}$	θ_{rot}	$\lvert a_S \rvert$	ϕ_S	$\lvert a_P \rvert$	ϕ_P	$\lvert a_D \rvert$	ϕ_D	$\lvert a_F \rvert$	ϕ_F
1.50	18	0.46 ± 0.01	122 ± 4	0.58 ± 0.04	55 ± 8	0.74 ± 0.02	138	0.07 ± 0.04	12 ± 23
1.54	12	0.25 ± 0.03	123 ± 6	0.65 ± 0.03	67 ± 5	0.38 ± 0.03	148	0.16 ± 0.03	34 ± 10
1.58	9	0.21 ± 0.03	129 ± 8	0.55 ± 0.03	78 ± 6	0.26 ± 0.02	154	0.21 ± 0.03	1 ± 12
1.62	17	0.25 ± 0.02	74 ±11	0.58 ± 0.02	80 ± 5	0.08 ± 0.05	162 ± 11	0.31 ± 0.02	24
1.66	2	0.24 ± 0.02	97 ± 9	0.52 ± 0.02	105 ± 5	0.11 ± 0.04	180 ± 10	0.33 ± 0.02	32
1.70	16	0.33 ± 0.02	79 ± 4	0.54 ± 0.01	106 ± 4	0.06 ± 0.02	79 ± 27	0.38 ± 0.02	45
1.74	10	0.36 ± 0.02	91 ± 3	0.53 ± 0.02	130 ± 3	0.13 ± 0.02	99 ± 9	0.41 ± 0.02	65
1.78	2	0.37 ± 0.02	106 ± 2	0.48 ± 0.02	152 ± 3	0.15 ± 0.02	113 ± 8	0.45 ± 0.02	90
1.82	- 5	0.50 ± 0.03	119 ± 2	0.42 ± 0.02	165 ± 5	0.21 ± 0.02	115 ± 7	0.44 ± 0.02	113
1.86	- 8	0.54 ± 0.03	131 ± 3	0.28 ± 0.03	168 ± 8	0.25 ± 0.03	112 ± 5	0.40 ± 0.03	130

Table 5

Resonance parameters for the non-leading I = 1/2 Kπ partial waves. These parameters have been estimated by ascribing circular motion in the Argand diagrams of Fig. 15 to resonances.

Partial Wave	Solution	A	B	C	D
0^+	M_R(MeV)	1400	1450	1400	1450
	Γ_R(MeV)	250	325	225	250
	x	0.8	0.9	0.5	0.8
1^-	M_R(MeV)	----	1650	----	1650
	Γ_R(MeV)	----	250	----	300
	x	<.05	0.3	<.05	0.25
2^+	M_R(MeV)	----	----	----	----
	Γ_R(MeV)	----	----	----	----
	x	<.02	<.02	<.02	<0.1

Figure Captions

1. The (unnormalized) t-channel moments of the $K^-\pi^+$ angular distribution in the t' range $0 < -t' < 0.15$ GeV^2 as a function of $M_{K\pi}$.
2. The (unnormalized t-channel moments of the $K^+\pi^+$ distribution in the t' range $0 < -t' < 0.15$ GeV^2 as a function of $M_{K\pi}$.
3. The (unnormalized) t-channel moments of the $K^+\pi^-$ angular distribution in the t' range $0 < -t' < 0.2$ GeV^2 as a function of $M_{K\pi}$. The data shown have not been corrected for the non-Δ^{++} background in the missing mass cut $1.0 < MM < 1.4$ GeV.
4. The (unnormalized) t-channel moments of the $K^-\pi^-$ angular distribution in the t' range $0 < -t' < 0.15$ GeV^2 as a function of $M_{K\pi}$. The data have been corrected for the non-Δ^{++} background in the missing mass cut $1.0 < MM < 1.4$ GeV.
5. The moments (unnormalized) of (a) the $K^-\pi^+$ angular distribution, and (b) the $K^+\pi^-$ angular distributions as a function of t' in the mass range $0.94 < M_{K\pi} < 1.0$ GeV. The curves represent the t-dependent amplitude parametrization described in section 3 of the text.
6. The $M_{K\pi}$ dependence of the parameters of Eqs. (6) and (9) to (12) describing the t dependence of (a) the $K\pi$n, and (b) the $K\pi\Delta$ production amplitudes. The open circles of Fig. 6a (6b) refer to $K^+\pi^+$ ($K^-\pi^-$) production, the solid points to $K^-\pi^+$ ($K^+\pi^-$) production. The curves are the polynomial fits used in the single t bin analyses of section 4.
7. The I=3/2 S wave phase shift calculated from (a) $K^+p \to K^+\pi^+n$ data, or (b) $K^-p \to K^-\pi^-\Delta^{++}$ data. The open circles were obtained by extrapolating the production amplitudes to $t=\mu^2$, the solid points are from the single t bin

analysis. The curves represent effective range fits with the parameter values of Table 1a.

8. The I=1/2 $K\pi$ phase shifts in the elastic region calculated from (a) $K^-p \to K^-\pi^+n$, or (b) $K^+p \to K^+\pi^-\Delta^{++}$ data. Open circles represent results from extrapolating to $t=\mu^2$, solid points come from the single t bin analysis. The input values of δ_S^3 were taken from the effective range curve of Fig. 7. The curves through δ_P^1 represent Breit-Wigner fits to the points from 0.8 to 1.0 GeV, yielding the resonance parameters shown in Table 1b. The curves through δ_S^1 represent effective range fits (for $M < 1.2$ GeV) yielding the parameters listed in Table 1c.

9. The (complex) zeros of the non-exotic $K\pi$ scattering amplitude as calculated from the partial waves of Figs. 12 and 13, resulting from the simultaneous analysis of $K^+\pi^-$ and $K^-\pi^+$ data. The solid points (open circles) represent the real (imaginary) parts of the zeroes. Either $\mathrm{Im}\, z_1$ and/or $\mathrm{Im}\, z_2$ could change sign at $M_{K\pi} \sim 1.5$ GeV.

10. The magnitudes and phases of the $K^-\pi^+$ partial waves. The curves for $|a_D|$ and ϕ_D represent Breit-Wigner fits to $|a_D|$ with the parameters listed in Table 1d. Below 1.3 GeV, the overall phase is fixed by elastic unitarity. For $1.3 < M_{K\pi} < 1.6$ GeV, ϕ_D is chosen to have the Breit-Wigner phase shown by the curve; for $M_{K\pi} > 1.6$ GeV, ϕ_F is chosen to have the values shown by the curve representing a resonance of mass 1.78 GeV, width 175 MeV. Below about 1.5 GeV, all four solutions are identical. Above 1.5 GeV, all solutions have $\mathrm{Im}\, z_3 < 0$, while in A $\mathrm{Im}\, z_1 < 0$ and $\mathrm{Im}\, z_2 < 0$; in B $\mathrm{Im}\, z_1 > 0$, $\mathrm{Im}\, z_2 < 0$; in C $\mathrm{Im}\, z_1 < 0$, $\mathrm{Im}\, z_2 > 0$; and in D $\mathrm{Im}\, z_1 > 0$, $\mathrm{Im}\, z_2 > 0$.

11. The magnitudes and phases of the $K^+\pi^-$ partial waves. The curves for $|a_D|$ and ϕ_D represent Breit-Wigner fits to $|a_D|$ with the parameters listed in Table 1d. The curve for ϕ_F represents the phase associated with a resonance of mass 1.78 GeV and width 175 MeV. For $M_{K\pi} < 1.3$ GeV, the overall phase is fixed by elastic unitarity. For $1.3 < M_{K\pi} < 1.6$ GeV, ($M_{K\pi} > 1.6$ GeV) the phases are measured relative to ϕ_D (ϕ_F) chosen to have the Breit-Wigner phase shown by the curve.

12. (a) The I=3/2 S wave $K\pi$ phase shift obtained from a simultaneous analysis of single t bin $K^-\pi^-$ and $K^+\pi^+$ data. The curve represents an effective range fit with the parameters listed in Table 1a. (b) The I=1/2 S and P wave $K\pi$ phase shifts obtained from the simultaneous $K^+\pi^-$ and $K^-\pi^+$ analysis of section 4.5 of the text. The input values of δ_S^3 were taken from the effective range curve of Fig. 12a. The curve through δ_S^1 represents an effective range fit (for $M_{K\pi} < 1.2$ GeV) yielding the parameters in Table 1c, while the parameters of the Breit-Wigner fit to δ_P^1 can be found in Table 1b.

13. The magnitudes and phases of the $K\pi$ partial waves calculated in a joint $K^+\pi^-/K^-\pi^+$ analysis. The curves for $|a_D|$ and ϕ_D represent Breit-Wigner fits to $|a_D|$ with the parameters listed in Table 1d. The curves for ϕ_F represent a Breit-Wigner description of an F-wave resonance of mass 1.78 GeV, width 175 MeV. Below 1.3 GeV, the overall phase is fixed by elastic unitarity. For $1.3 < M_{K\pi} < 1.6$ GeV ($M_{K\pi} > 1.6$ GeV) ϕ_D (ϕ_F) is chosen to have the Breit-Wigner phase shown by the curve. Below about 1.5 GeV, all four solutions are identical. Above 1.5 GeV, the four solutions are classified according to their Barrelet zeros.

14. The magnitudes and phases of the S and P partial waves of Solution B as calculated from the combined $K^-\pi^+n$ and $K^+\pi^-\Delta^{++}$ single t bin analysis of

section 4.5. The choice of overall phase in the inelastic region is identical to that of Fig. 13. The solid S wave curves correspond to effective range fits to δ_s^1 and δ_s^3. The dashed curves above 1.2 GeV are extrapolations of these curves and the dashed-dotted curve represents the I=3/2 S wave contribution to $|a_s|$. The P wave curves correspond to a Breit-Wigner resonance fit to δ_p for $0.8 < M_{K\pi} < 1.0$ GeV and the extrapolation of this fit outside that $M_{K\pi}$ region.

15. Argand plots for solutions A-D from a combined $K^+\pi^-/K^-\pi^+$ partial wave analysis. The points for $M_{K\pi} > 1.48$ GeV, plotted at 40 MeV intervals, were calculated using data in overlapping 120 MeV $M_{K\pi}$ bins. At each point, the overall phase was chosen, as far as possible, to satisfy unitarity, continuity, and approximately Breit-Wigner behavior for the leading 2^+ and 3^- resonances. The diameters of the unitarity circles are $\sqrt{2L+1}$. The I=1/2 S wave was obtained by subtracting from the full S wave amplitude the I=3/2 S wave amplitude calculated from the effective range curve of Fig. 12a.

16. Argand diagrams and projections of the real and imaginary parts of the $K\pi$ partial waves of solution B obtained from a combined $K^+\pi^-/K^-\pi^+$ partial wave analysis. For $M_{K\pi} < 1.3$ GeV, the points are calculated from the phase shift results of Fig. 12b (and Table 3b). The points for $M_{K\pi} > 1.3$ GeV are the same as those of Fig. 15. The unitarity circles are chosen to have unit diameter. The S wave plotted is the I=1/2 S wave obtained by subtracting from the full S wave amplitude the I=3/2 amplitude obtained from the effective range curve of Fig. 12a.

17. Predictions for the $L<4$ moments of the $\bar{K}^0\pi^0$ angular distribution in the reaction $K^-p \to \bar{K}^0\pi^0 n$ at 13 GeV/c in the region $|t'| < 0.15$ GeV^2, as

calculated from our $K\pi$ partial wave results. The $L > 3$ moments are the same for all four solutions and equal to one half the corresponding $K^-p \rightarrow K^-\pi^+n$ moments of Fig. 1. The shaded bands shown for each of the four solutions represent the range of values obtained if the overall phase of Fig. 15 is changed by $\pm 10^o$. Below 1.46 GeV the overall phase is fixed by the imposition of elastic unitarity.

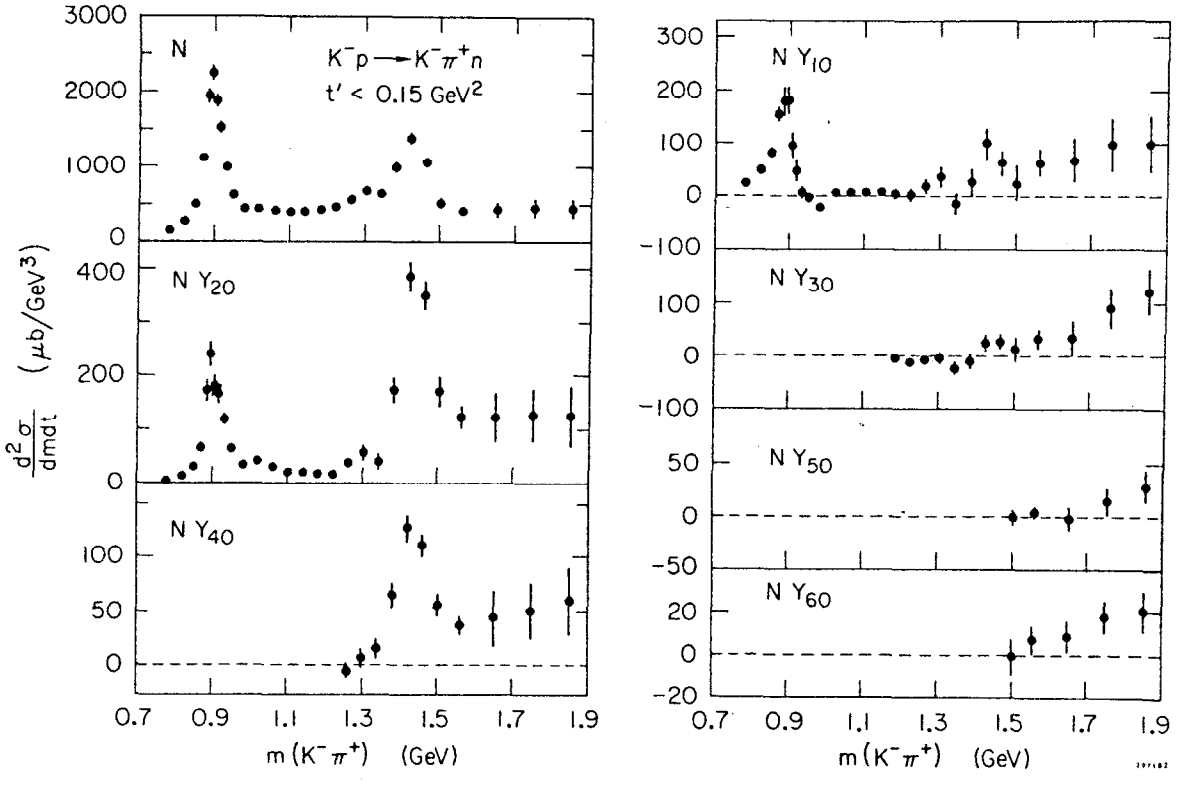
N
$K^-p \rightarrow K^-\pi^+n$
$t' < 0.15\ GeV^2$
N Y_{20}
N Y_{40}
N Y_{10}
N Y_{30}
N Y_{50}
N Y_{60}
$\frac{d^2\sigma}{dmdt}$ ($\mu b/GeV^3$)
$m(K^-\pi^+)$ (GeV)
$m(K^-\pi^+)$ (GeV)

Fig. 1

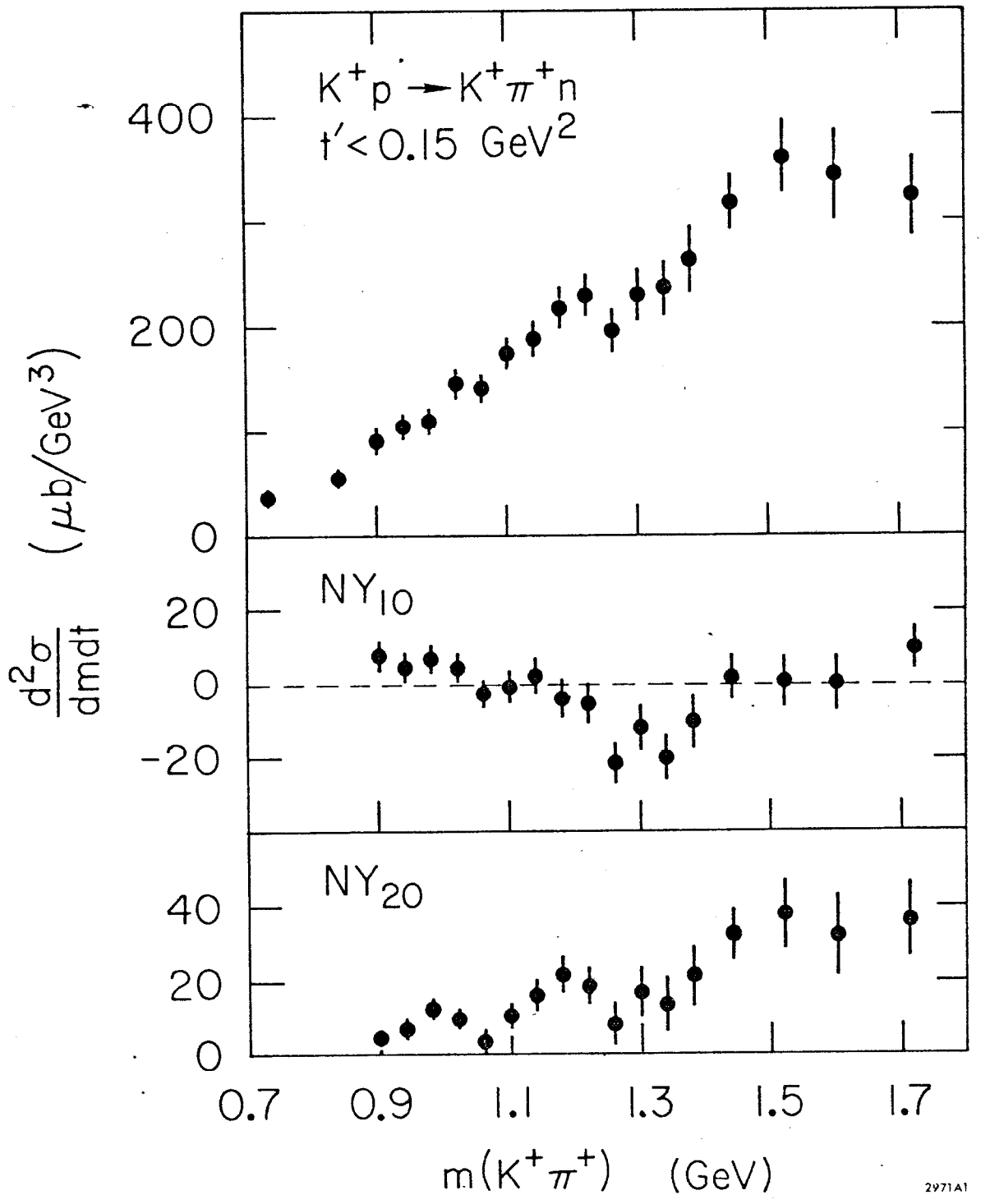
$K^+p \to K^+\pi^+n$
$t' < 0.15$ GeV^2
400
200
0
$\frac{d^2\sigma}{dmdt}$ (μb/GeV^3)
NY$_{10}$
20
0
-20
NY$_{20}$
40
20
0
0.7
0.9
1.1
1.3
1.5
1.7
m($K^+\pi^+$) (GeV)
2971A1

Fig. 2

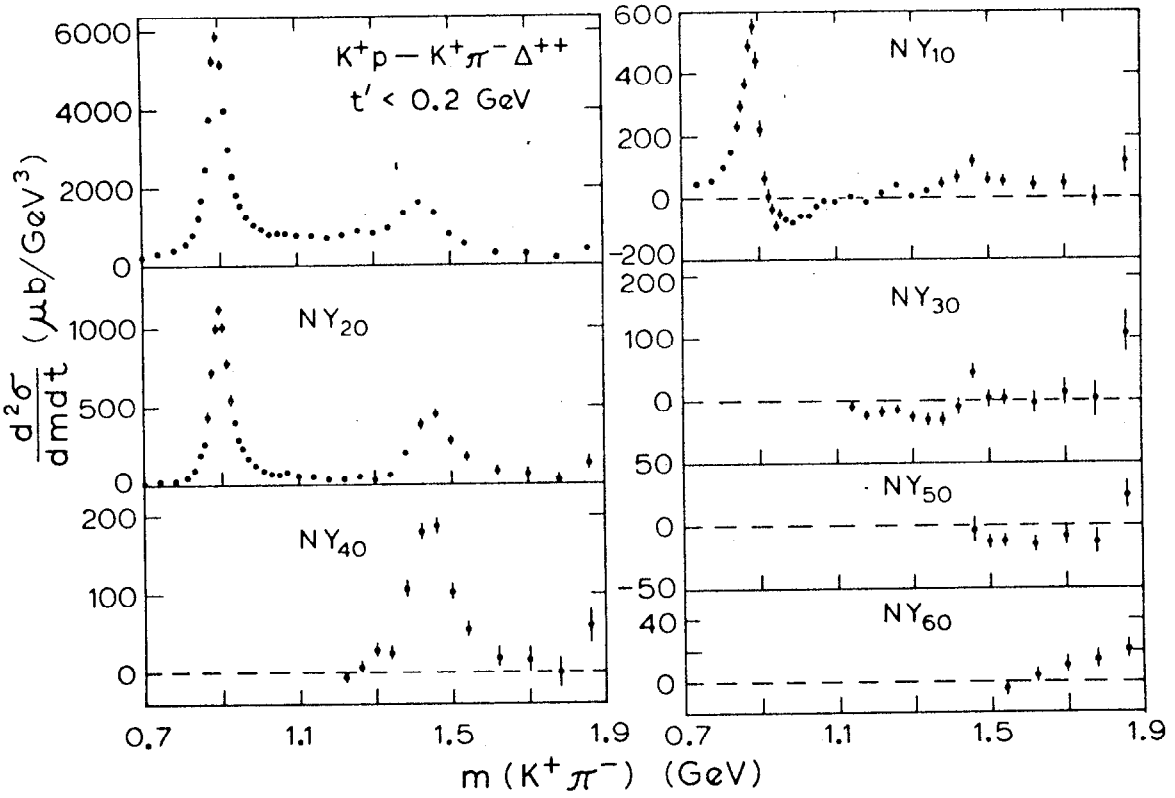
$K^+p - K^+\pi^-\Delta^{++}$
$t' < 0.2$ GeV
NY_{10}
NY_{20}
NY_{30}
NY_{40}
NY_{50}
NY_{60}
$\frac{d^2\sigma}{dmdt}$ (μb/GeV^3)
m ($K^+\pi^-$) (GeV)

Fig. 3

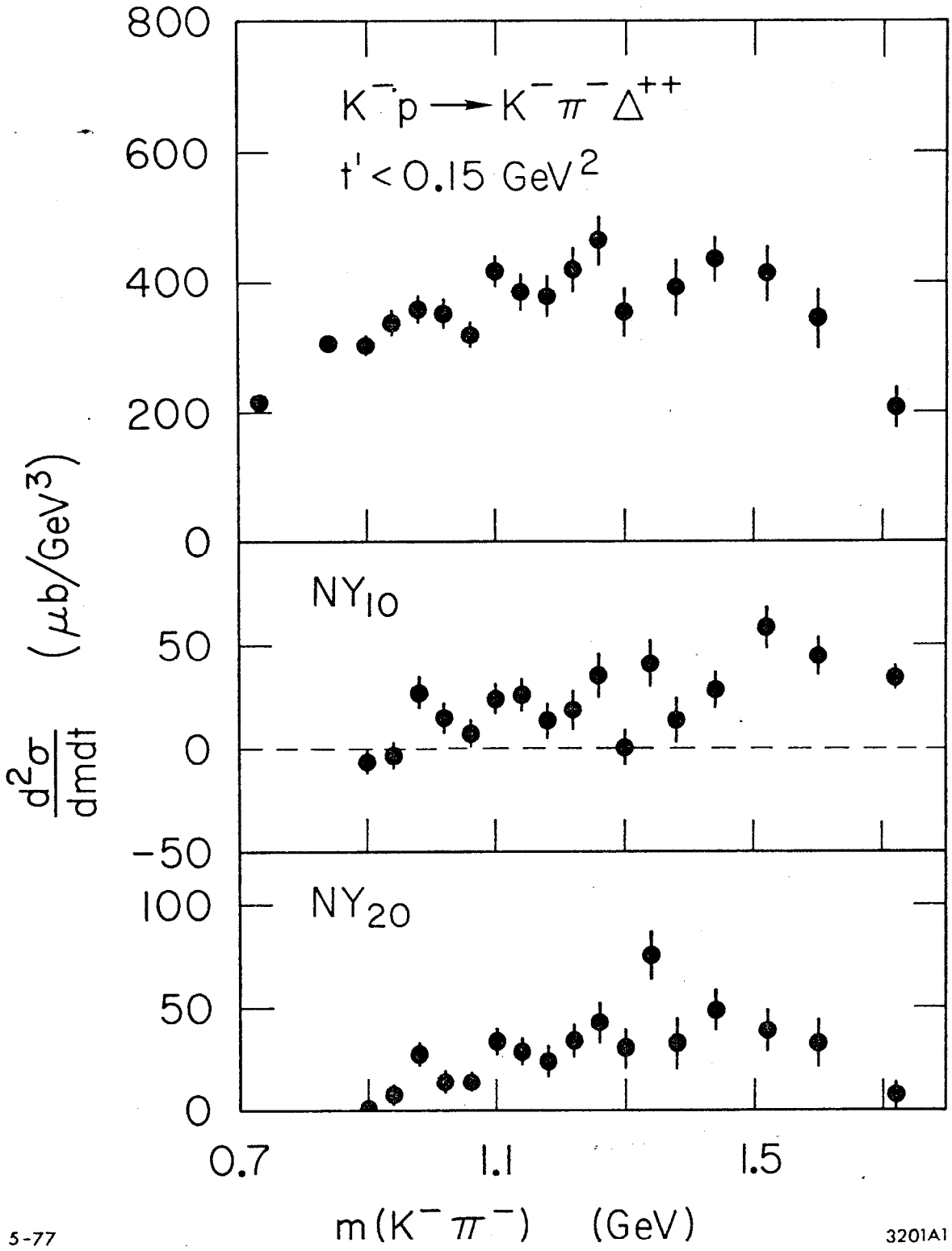
800
600
400
200
0
$K^- p \rightarrow K^- \pi^- \Delta^{++}$
$t' < 0.15$ GeV^2
NY10
50
0
-50
100
NY20
50
0
0.7
1.1
1.5
$\frac{d^2\sigma}{dmdt}$ (μb/GeV^3)
m($K^- \pi^-$) (GeV)
5-77
3201A1

Fig. 4

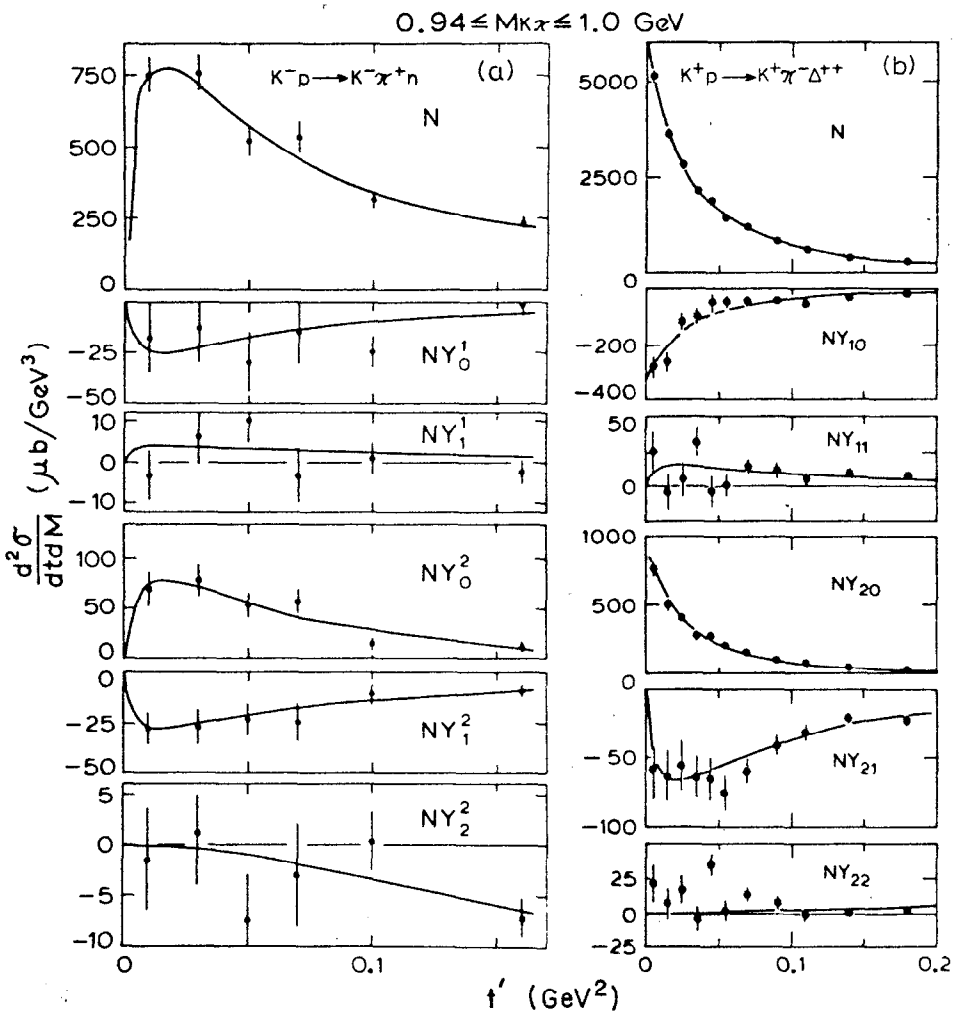
0.94 ≤ MKπ ≤ 1.0 GeV
K⁻p → K⁻π⁺n
(a)
N
NY¹₀
NY¹₁
NY²₀
NY²₁
NY²₂
K⁺p → K⁺π⁻Δ⁺⁺
(b)
N
NY₁₀
NY₁₁
NY₂₀
NY₂₁
NY₂₂
d²σ/dtdM (μb/GeV³)
t′ (GeV²)

Fig. 5

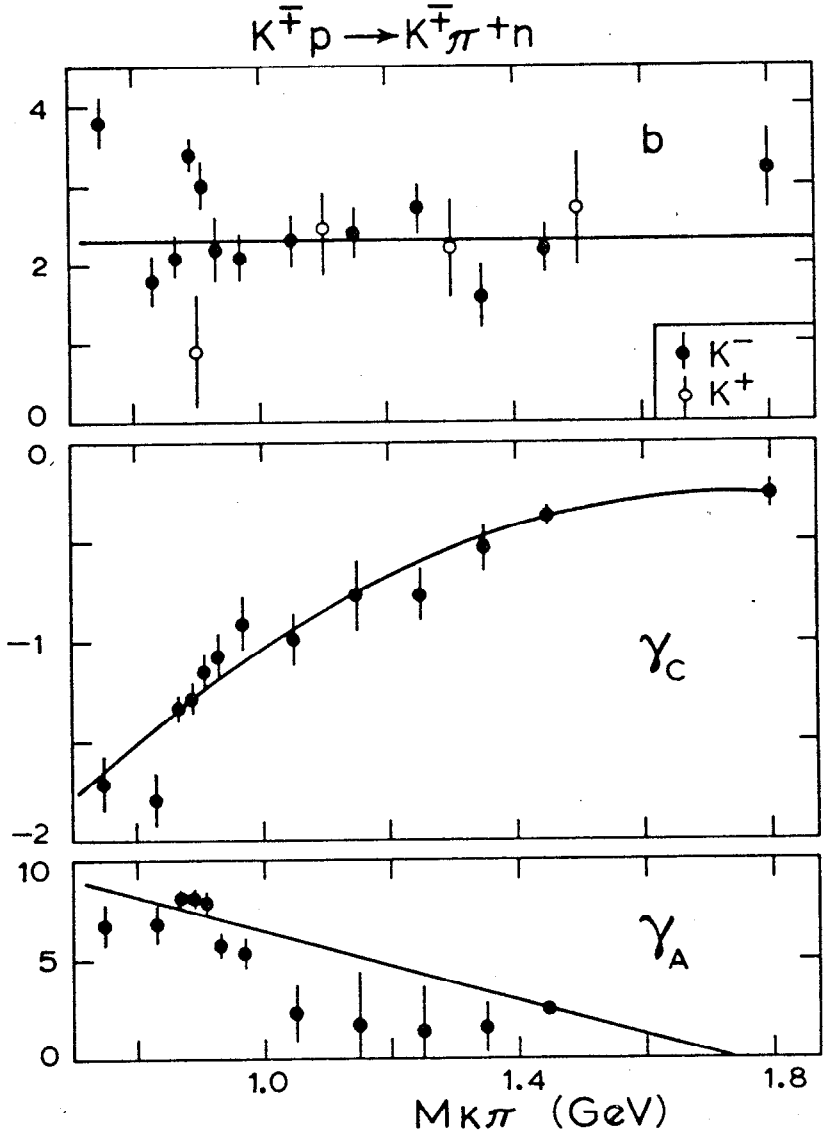
$K^{\mp}p \rightarrow K^{\mp}\pi^{+}n$
b
K^-
K^+
γ_C
γ_A
4
2
0
0
−1
−2
10
5
0
1.0
1.4
1.8
$M_{K\pi}$ (GeV)

Fig. 6a

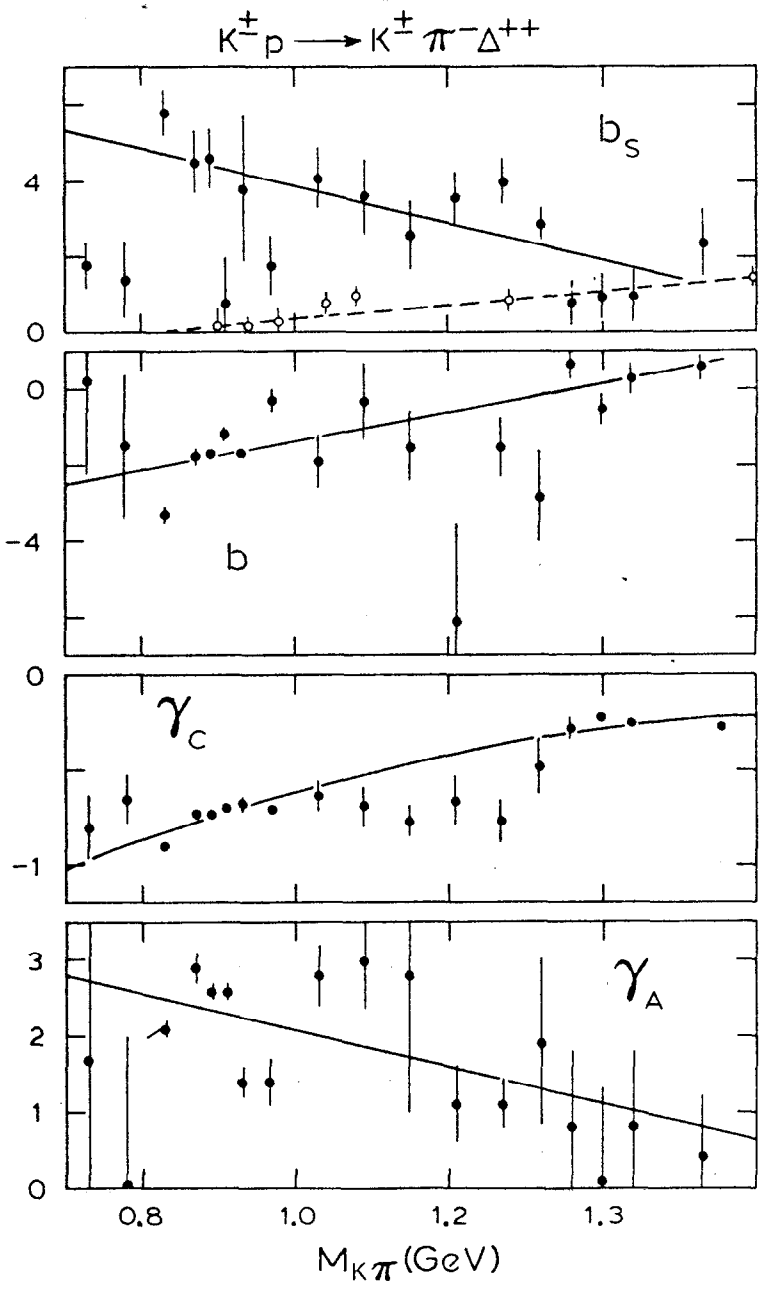
$K^{\pm}p \longrightarrow K^{\pm}\pi^{-}\Delta^{++}$
b_S
b
γ_C
γ_A
4
0
0
-4
0
-1
3
2
1
0
0.8
1.0
1.2
1.3
$M_{K\pi}$(GeV)

Fig. 6b

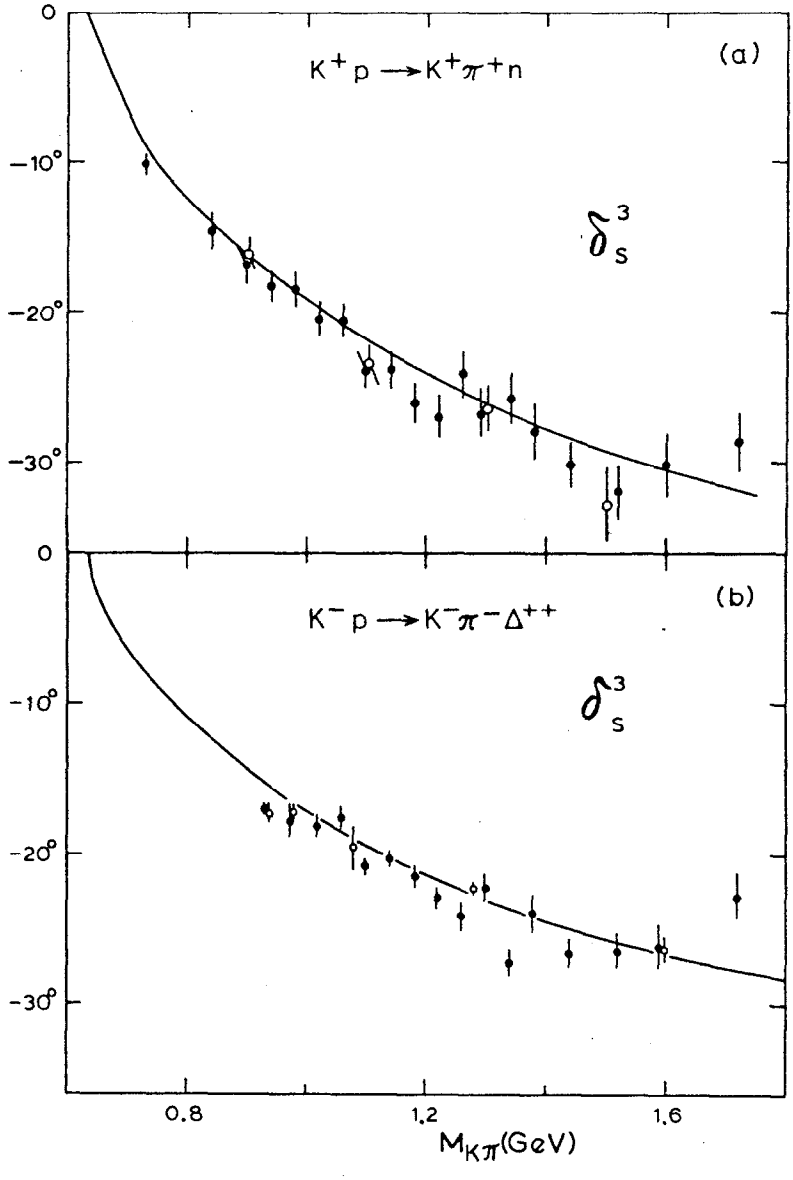
0
−10°
−20°
−30°
$K^+p \rightarrow K^+\pi^+n$
(a)
δ_s^3
0
−10°
−20°
−30°
$K^-p \rightarrow K^-\pi^-\Delta^{++}$
(b)
δ_s^3
0.8
1.2
1.6
$M_{K\pi}$(GeV)

Fig. 7

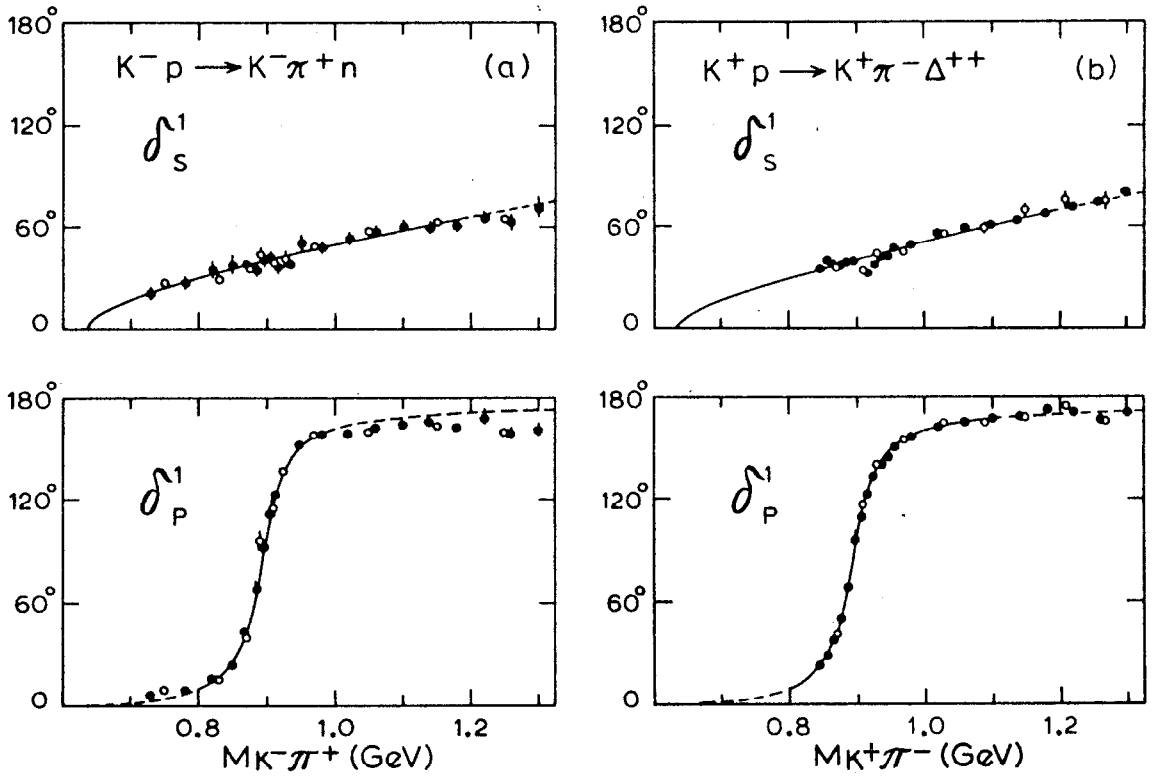
180°
120°
60°
0
$K^- p \rightarrow K^- \pi^+ n$
(a)
δ^1_S
δ^1_P
$K^+ p \rightarrow K^+ \pi^- \Delta^{++}$
(b)
0.8
1.0
1.2
$M_{K^-\pi^+}$ (GeV)
$M_{K^+\pi^-}$ (GeV)

Fig. 8

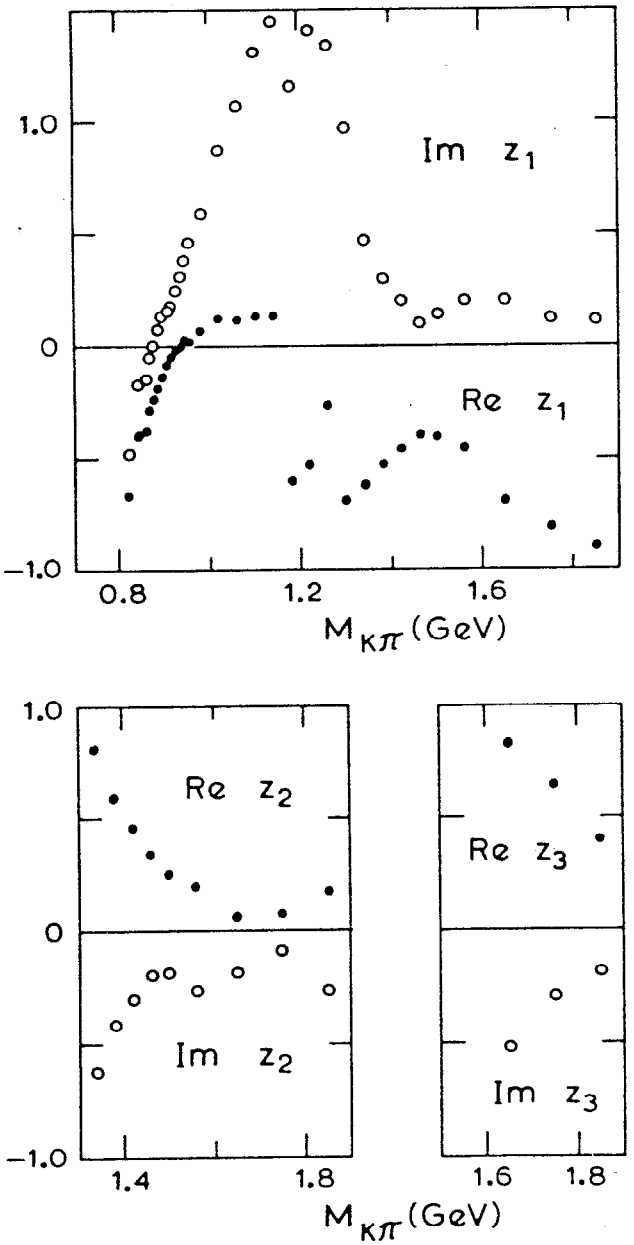
1.0
0
−1.0
Im z1
Re z1
0.8
1.2
1.6
MKπ (GeV)
1.0
0
−1.0
Re z2
Im z2
Re z3
Im z3
1.4
1.8
1.6
1.8
MKπ (GeV)

Fig. 9

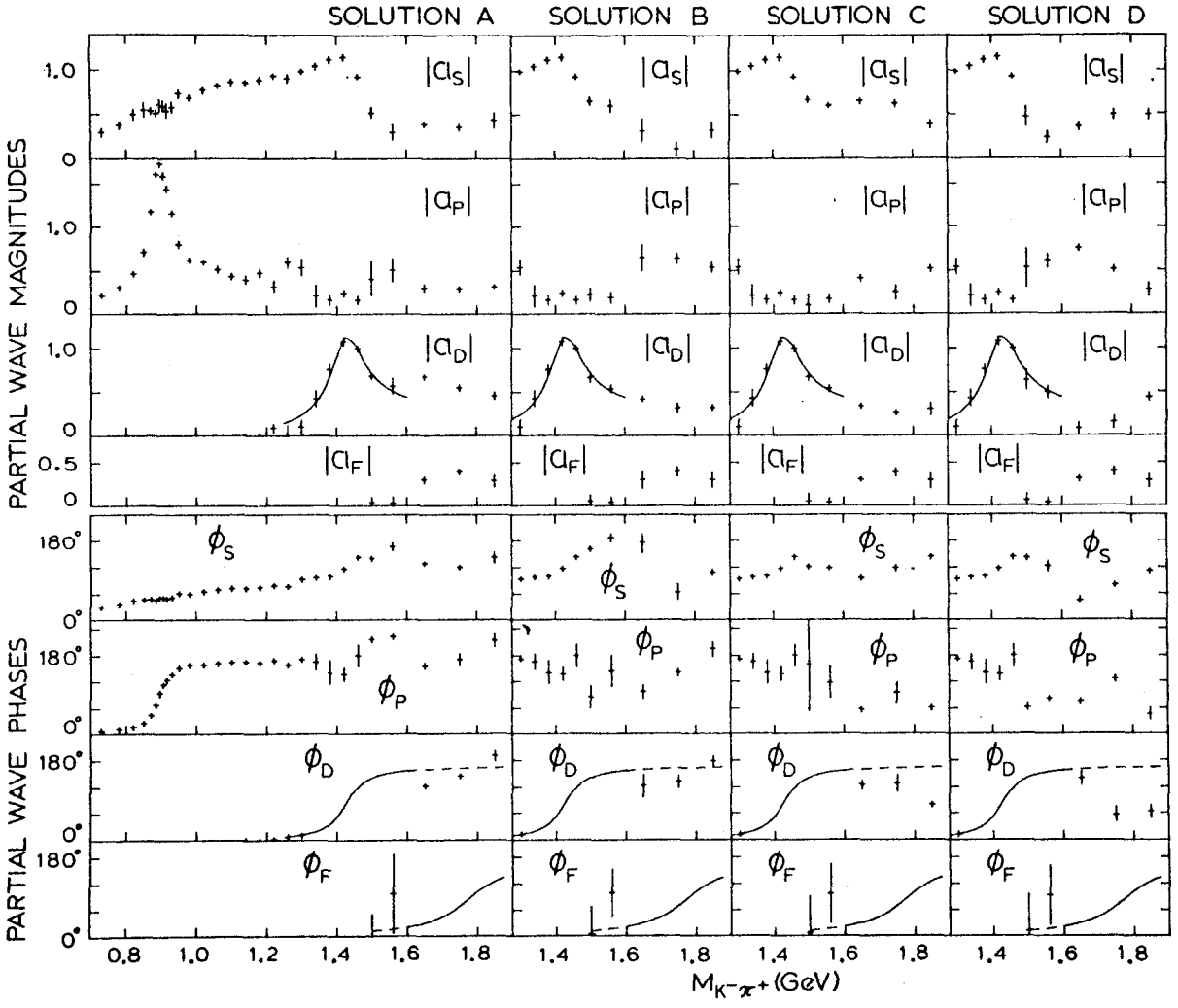
SOLUTION A
SOLUTION B
SOLUTION C
SOLUTION D
PARTIAL WAVE MAGNITUDES
PARTIAL WAVE PHASES
$|a_S|$
$|a_P|$
$|a_D|$
$|a_F|$
ϕ_S
ϕ_P
ϕ_D
ϕ_F
1.0
0
0.5
180°
0°
0.8
1.0
1.2
1.4
1.6
1.8
$M_{K^-\pi^+}$ (GeV)

Fig. 10

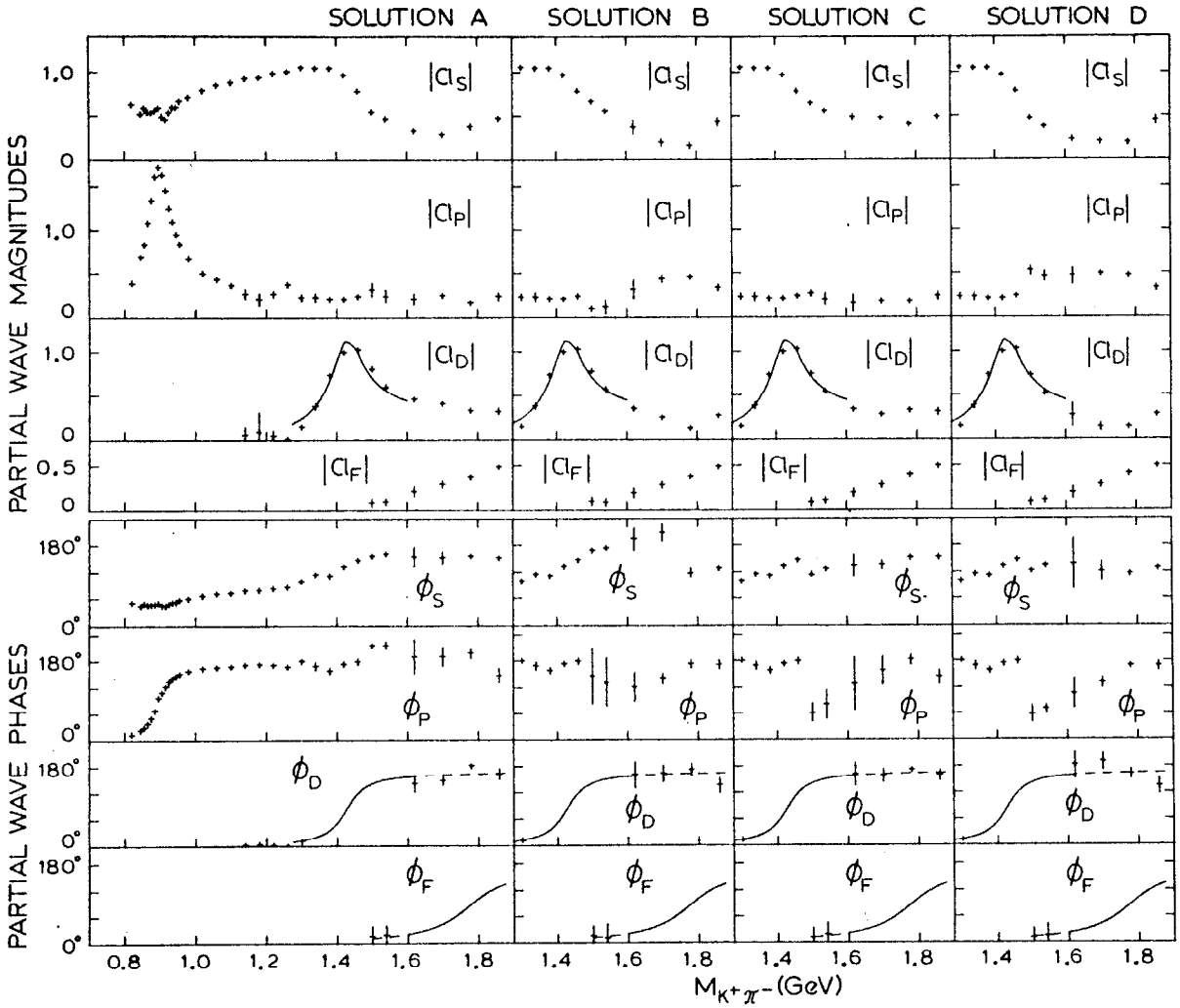
SOLUTION A
SOLUTION B
SOLUTION C
SOLUTION D
PARTIAL WAVE MAGNITUDES
PARTIAL WAVE PHASES
$|a_S|$
$|a_P|$
$|a_D|$
$|a_F|$
ϕ_S
ϕ_P
ϕ_D
ϕ_F
1.0
0
0.5
180°
0°
0.8
1.0
1.2
1.4
1.6
1.8
$M_{K^+\pi^-}$(GeV)

Fig. 11

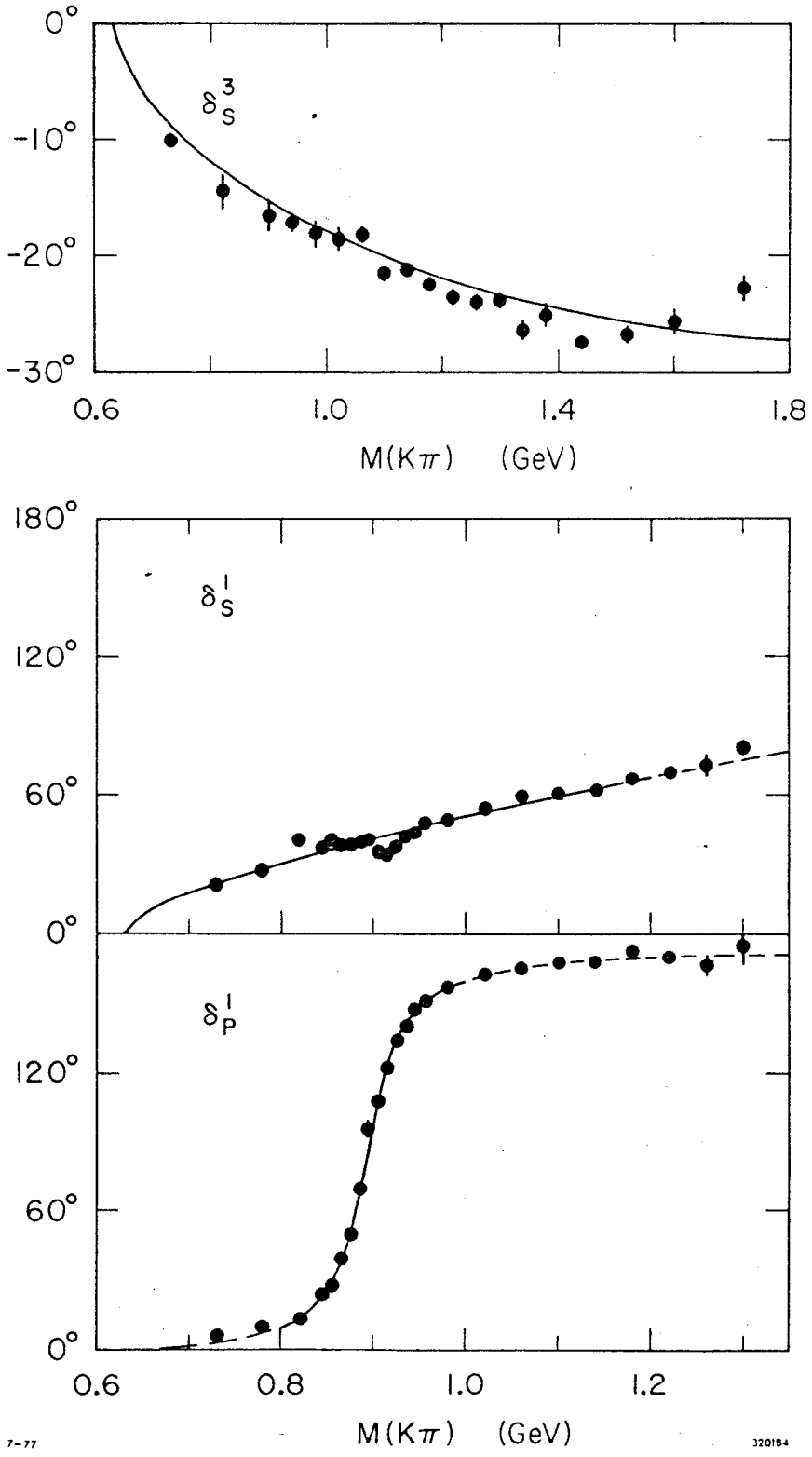
0°
-10°
-20°
-30°
δ_S^3
0.6
1.0
1.4
1.8
M(Kπ) (GeV)
180°
120°
60°
0°
δ_S^1
δ_P^1
120°
60°
0°
0.6
0.8
1.0
1.2
M(Kπ) (GeV)
7-77
3201B4

Fig. 12

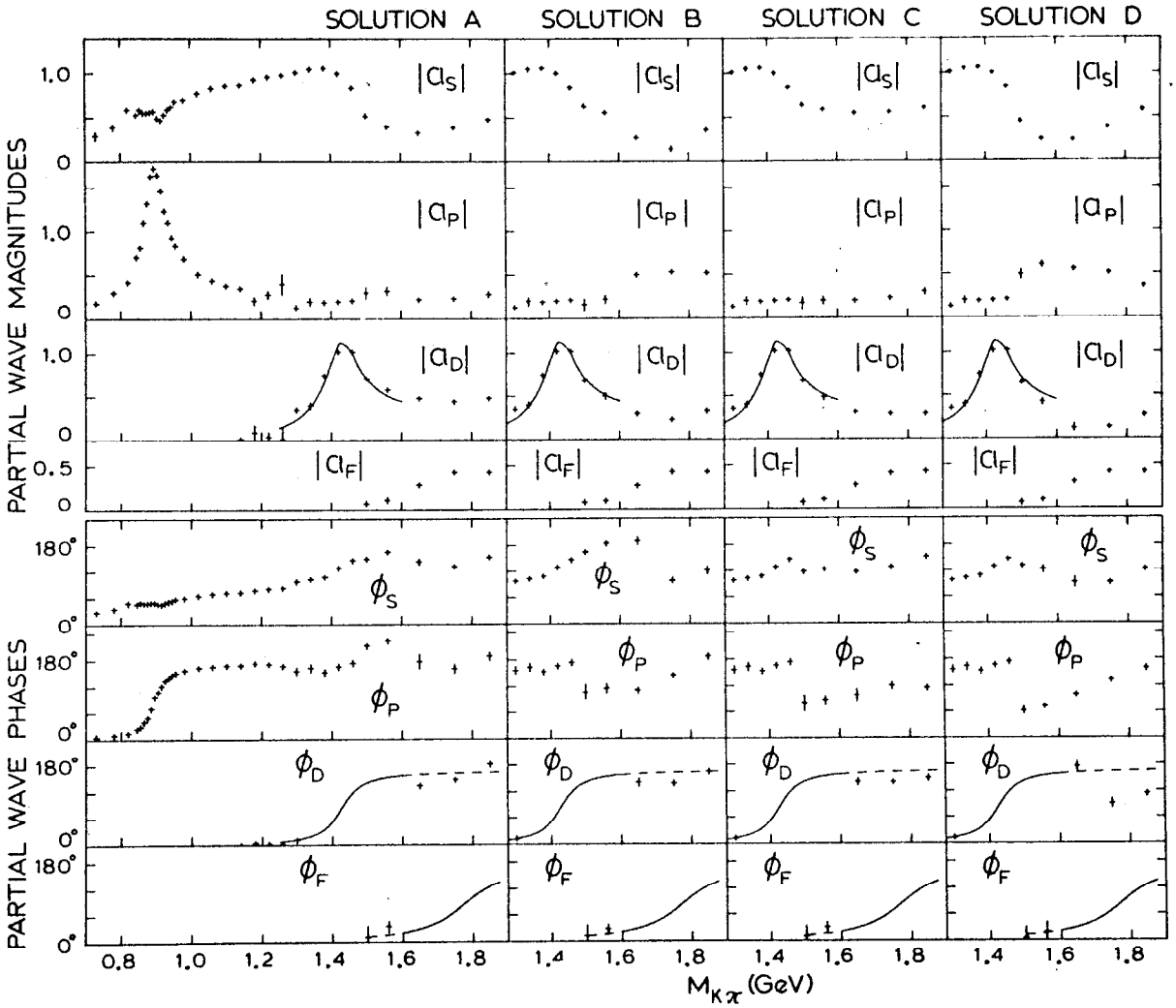
SOLUTION A
SOLUTION B
SOLUTION C
SOLUTION D
PARTIAL WAVE MAGNITUDES
PARTIAL WAVE PHASES
$|a_S|$
$|a_P|$
$|a_D|$
$|a_F|$
ϕ_S
ϕ_P
ϕ_D
ϕ_F
1.0
0
0.5
180°
0°
0.8
1.0
1.2
1.4
1.6
1.8
$M_{K\pi}$ (GeV)

Fig. 13

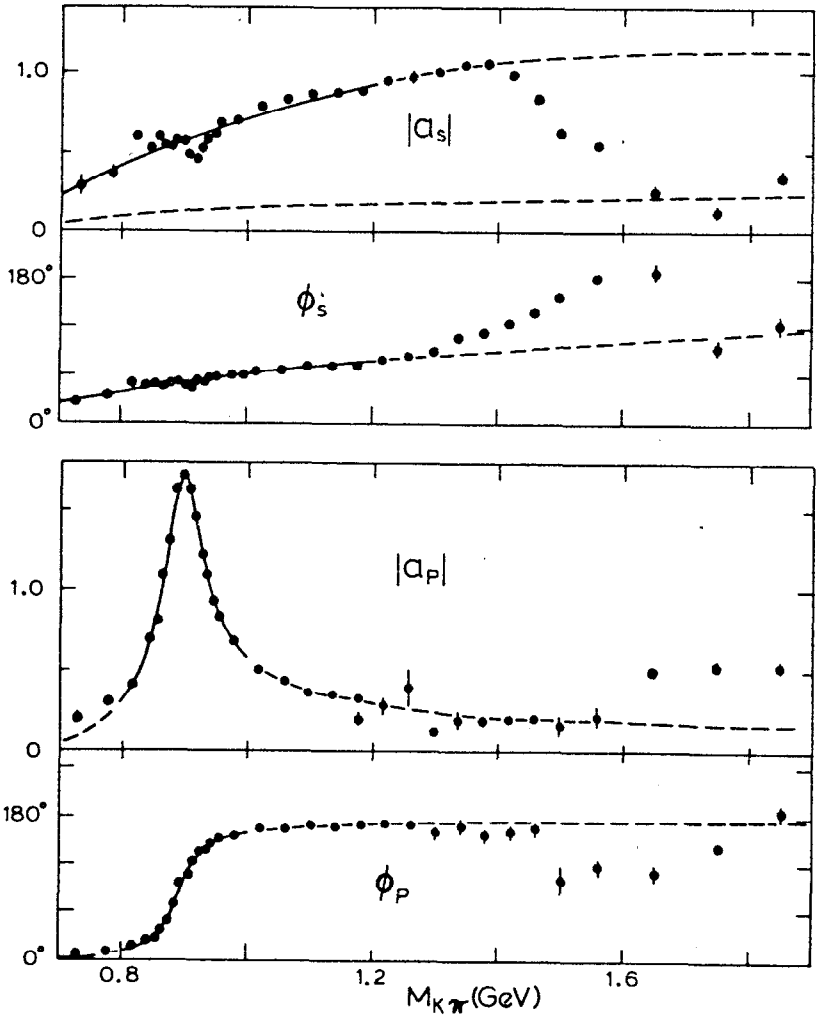

Fig. 14

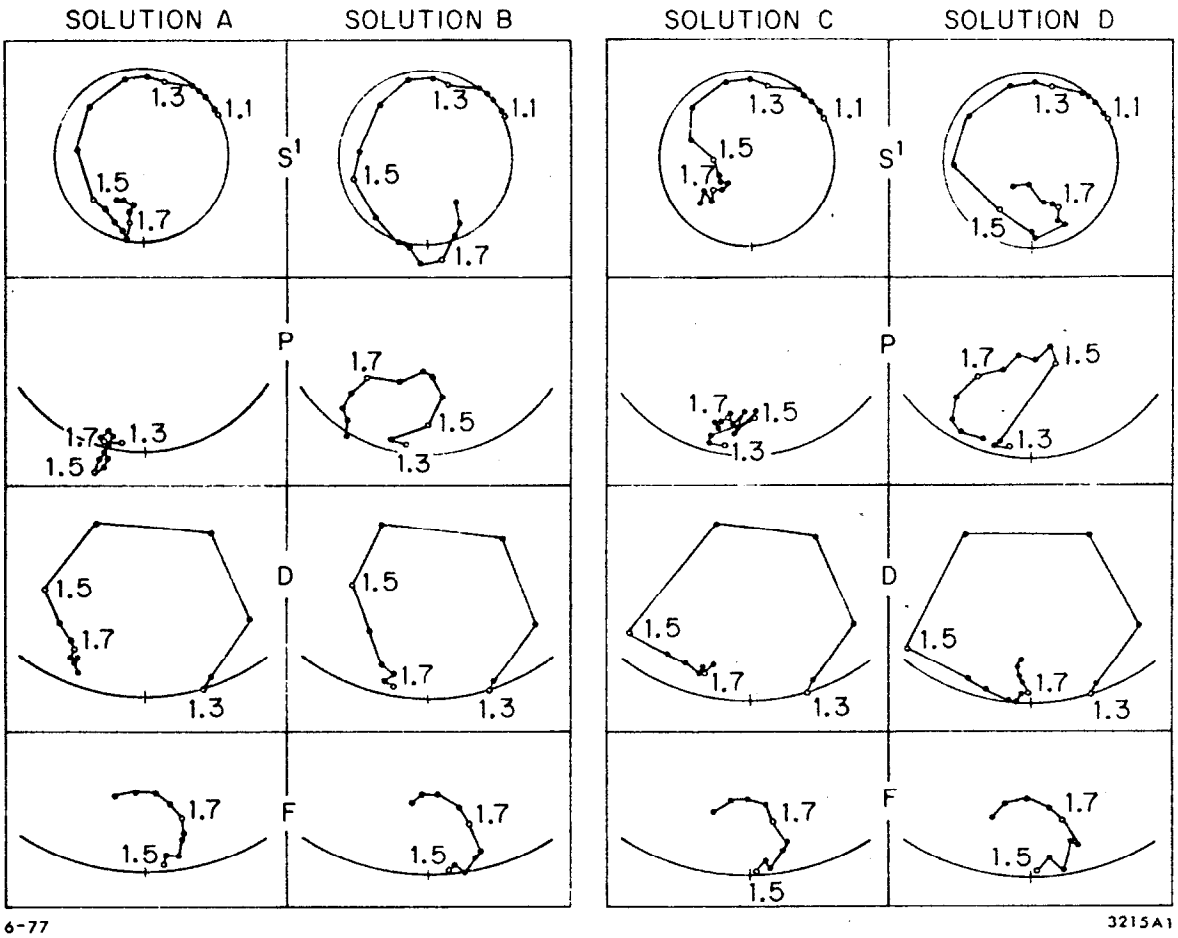
SOLUTION A
SOLUTION B
SOLUTION C
SOLUTION D
S1
P
D
F
1.1
1.3
1.5
1.7
N
6-77
3215A1

Fig. 15

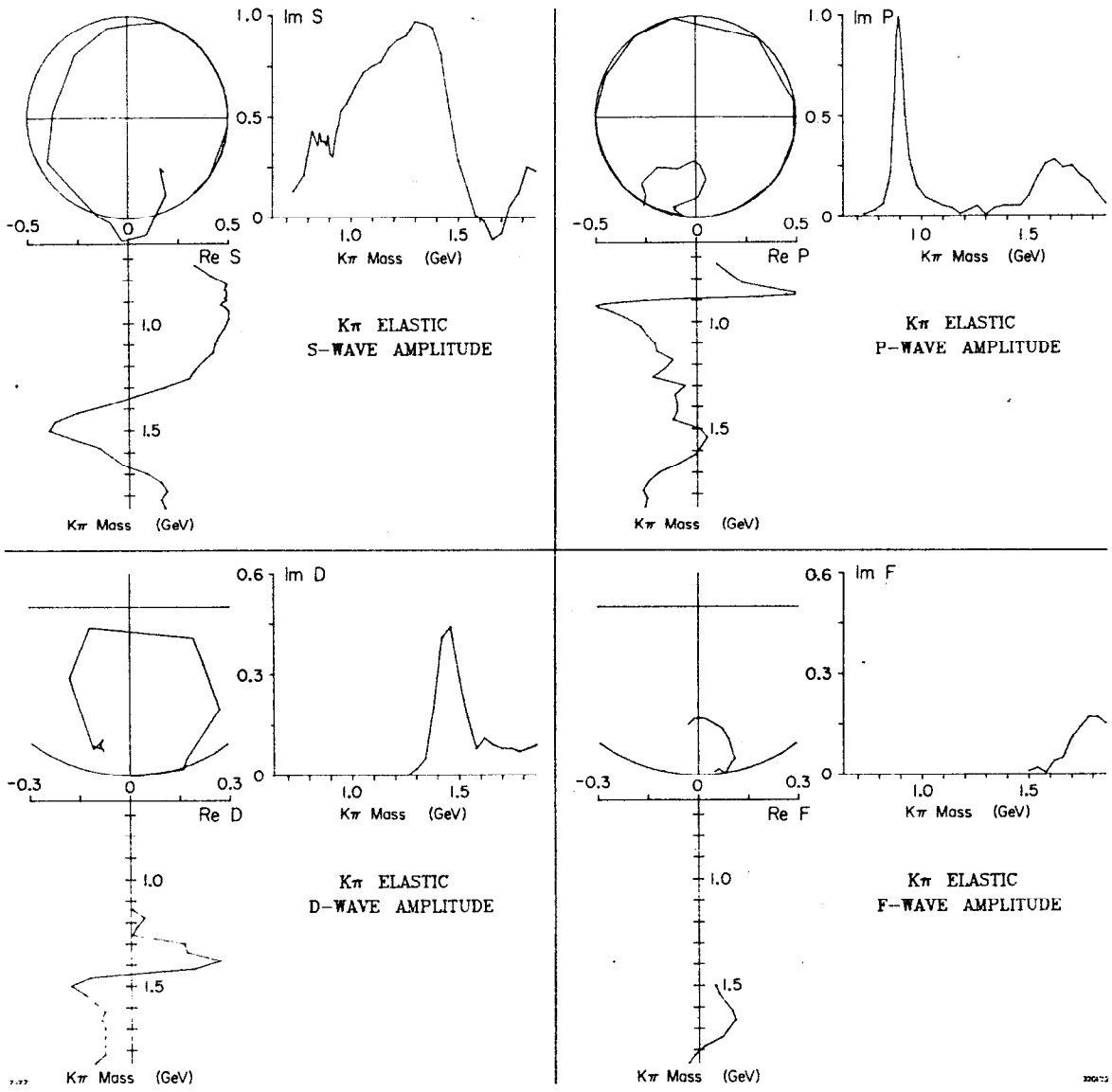
Im S
Re S
Kπ Mass (GeV)
Kπ ELASTIC
S-WAVE AMPLITUDE
Im P
Re P
Kπ Mass (GeV)
Kπ ELASTIC
P-WAVE AMPLITUDE
Im D
Re D
Kπ Mass (GeV)
Kπ ELASTIC
D-WAVE AMPLITUDE
Im F
Re F
Kπ Mass (GeV)
Kπ ELASTIC
F-WAVE AMPLITUDE

Fig. 16

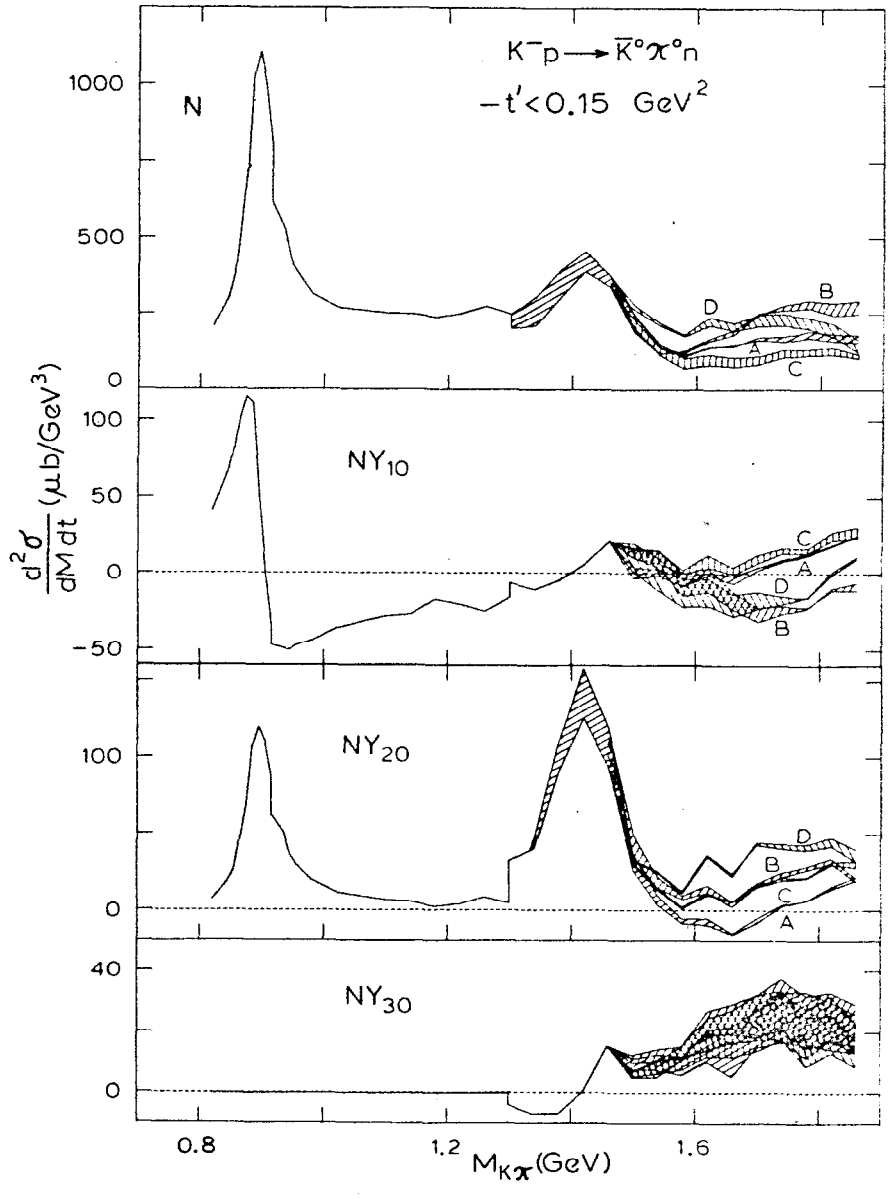
$K^-p \rightarrow \bar{K}^0\pi^0 n$
$-t' < 0.15$ GeV^2
N
NY_{10}
NY_{20}
NY_{30}
A
B
C
D
1000
500
0
100
50
0
-50
100
0
40
0
0.8
1.2
1.6
$M_{K\pi}$(GeV)
$\frac{d^2\sigma}{dM\,dt}$ (μb/GeV^3)

Fig. 17